

Contents

Introduction	3
1 Theoretical Background	7
Micro/Meso-scopic model	8
1.1 Gross-Pitaevskii model	8
1.2 Quantized vortex	9
1.3 Vortex filament model	10
1.4 Vortex dynamics	12
Macroscopic model	15
1.5 Hydrodynamics of superfluid	15
1.6 Dynamical similarity principle	17
1.7 Oscillatory flows	19
1.8 Quantum turbulence	21
2 Experimental Approach	24
2.1 Apparatus	24
2.2 Resonators	26
3 Simulations	30
3.1 Vortex filament model	30
3.2 Implementation	33
3.3 Time evolution	36
3.4 Re-segmentation of vortex	38
3.5 Future implementations	39

4 Results	41
4.1 Simulation experiments	41
4.2 Drag force experiments	47
5 Conclusions (2 pgs)	48
Bibliography	49

Introduction

To this day, turbulent motion of fluids remains the last unresolved problem of classical physics. They present many practical challenges across different areas of industry (f.e. weather prediction). Quantum turbulence, in contrast, may occur only in superfluids and was first observed in superfluid state of ^4He . Compared to classical turbulence, it can be regarded as a simpler system from the theoretical and numerical point of view. Also, it shares many of the general properties of turbulence in classical viscous fluids.

In very low temperatures, the liquid state of ^4He exists in two phases:

- Helium-I: a high temperature phase ($2.17\text{ K} < T < 4.2\text{ K}$)
- Helium-II: a low temperature phase ($T < 2.17\text{ K}$)

These two phases are connected with the *lambda transition*, which occurs at the critical temperature $T_\lambda = 2.17\text{ K}$ at saturated vapour pressure (**Figure 1**). Helium-I is a classical fluid described by ordinary Navier-Stokes (N-S) equations, whereas Helium-II is a superfluid and behaves partly like a Bose-Einstein condensate.

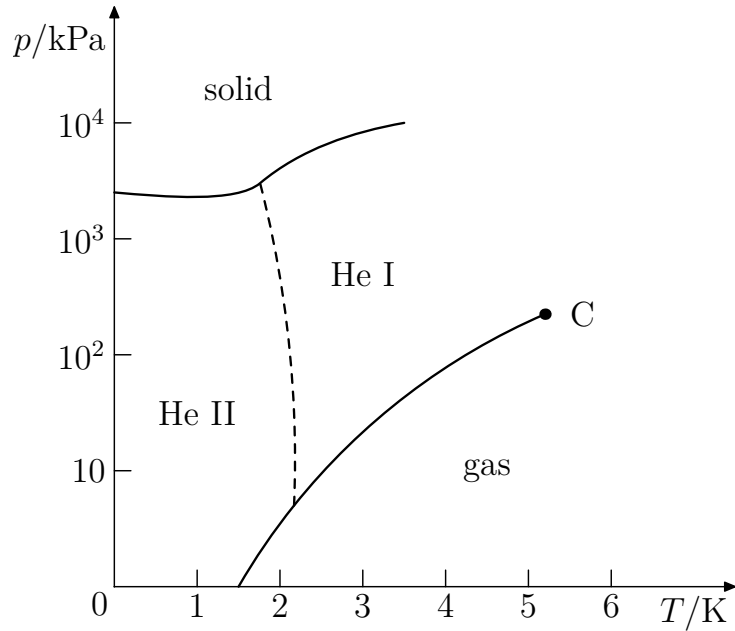


Figure 1: Pressure-Temperature diagram of ^4He . Fixing pressure on an atmospheric value, a gas-liquid transition is present at 4.2 K (He-I) and a superfluid transition at 2.17 K .

A simple, phenomenological model of the Helium-II motion was proposed by Tisza [1] and Landau [2] - the *two-fluid model*. According to two-fluid model, it behaves as if

composed of two inter-penetrating liquids - the normal and superfluid components - with corresponding velocity fields and temperature-dependent densities:

- normal component: density $\rho_n(T)$, velocity field $\mathbf{v}_n(\mathbf{r}, t)$, motion described by an ordinary viscous Navier-Stokes equation, carrying entropy and represented as a collection of thermal excitations such as *phonons* and *rotons*
- superfluid component: density $\rho_s(T)$, velocity field $\mathbf{v}_s(\mathbf{r}, t)$, motion described by a modified Euler equation (without viscosity) with quantum terms, no entropy and represented by a macroscopic wave function

The total density of Helium-II sums up to $\rho = \rho_n(T) + \rho_s(T) \approx \text{const}$ and the relative proportion of normal/superfluid component is determined mainly by the temperature (**Figure 2**). Near $T \rightarrow 0$ Helium-II becomes entirely superfluid $\rho_s/\rho \rightarrow 1$. The temperature dependence of this ratio is highly nonlinear. For example, the ratio ρ_n/ρ drops from 100% at 2.17 K to 50% at 1.95 K, to < 5% at 1.3 K, and is effectively negligible under 1 K.

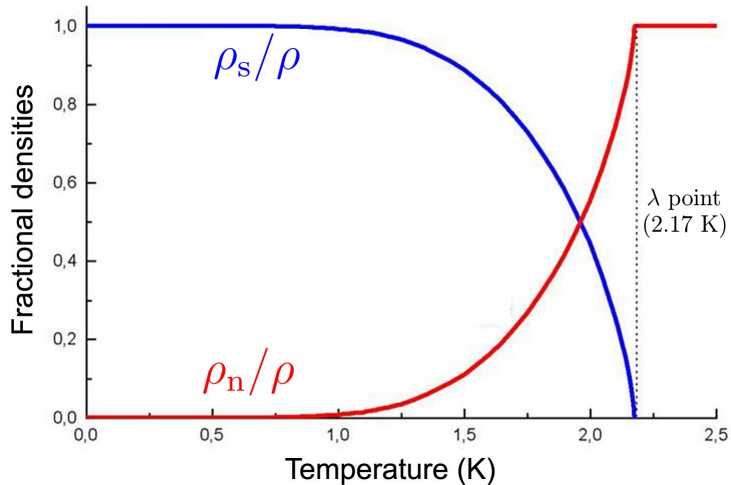


Figure 2: Temperature dependence of fractional densities of the normal (red) and superfluid (blue) components. Source: [3]

It arises from the quantum nature of superfluid, that the superfluid component should not perform any rotation. However, when this component moves faster than a critical velocity, the circulation is *quantized* and so-called *quantized vortices* are created, which makes the hydrodynamics of Helium-II particularly interesting. The vortex nucleation process is still a subject of many current investigations. Superfluid vortex lines were observed spatially organized, but also completely disorganized as simulated in **Figure 3**. Quantum turbulence therefore takes the form of a tangle of quantized vortices in the

superfluid component which typically coexist with classical turbulent flow of the normal component.

In the presence of quantized vortices, the independent normal and superfluid velocity fields become coupled by the *mutual friction* force which arises due to quasiparticles scattering off the cores of vortices.

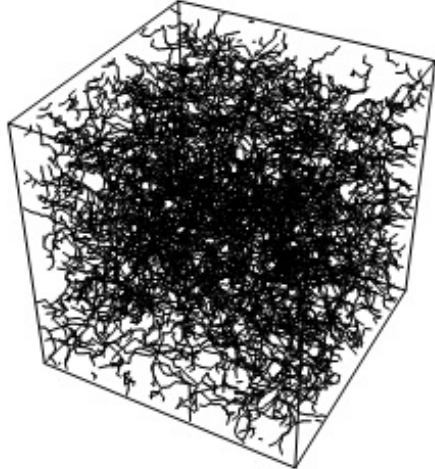


Figure 3: Cube of numerically simulated tangle of randomly distributed quantised vortices. Source: [3]

Also we note that for a typical experiment, below $\sim 0.7\text{ K}$, a transition to ballistic regime occurs in the normal component, as the mean free path of phonons exceeds the characteristic dimensions of the experimental setup. This situation is similar to the one of dilute classical gases.

Quantum turbulence can be experimentally achieved in many traditional ways - driving a mass flow, spinning discs, oscillating grids and forks, ultrasound and jets.

To characterize the turbulence one may use a superfluid Reynolds number for a steady flows, or a newly introduced [4] Donnelly number for high-frequency oscillatory flows. We find that for quantum turbulence originated in high-frequency regime above temperature $T > 1\text{ K}$, the measured drag forces are described in terms of a single dimensionless parameter and exhibit an universal scaling behaviour. We identify and compare the critical conditions related to the production of both quantized vorticity and instabilities occurring in normal component.

Besides experimental approaches on quantum fluids, one of the useful tools for understanding the geometry and flow of quantum turbulence, is the *vortex filament model*, pioneered by Schwarz [22]. With the rapid development of available computational power, large simulations have become the methods of choice for calculating the motion of fluids. In superfluids like Helium-II, due to the quantization of circulation, vorticity can

only exist within vortex filaments with a certain core size, which makes the model highly applicable.

We propose an efficient numerical method to compute the time evolution of vortex filaments in superfluid Helium-II. We studied the performance and stability and well replicated the physical processes such as the annihilation of quantized vortex rings [5] while travelling across superfluid.

We also present the `PyVort` code, a new platform in Python 3 to simulate quantized rings phenomena. More on the implementation part can be found in **Simulation** and **Appendix**.

Motivations and Goals

Here we briefly collect all motivations and goals that led us to our investigations.

Experimental approach

- investigate transition from laminar and potential flow of normal and superfluid components, respectively, to classical or quantum turbulence at various temperatures above $> 1 \text{ K}$ in high-frequency regime.
- construct an experiment using flow generators such as vibrating wire, tuning fork and oscillating disc and observe the drag phenomena
- apply universal scaling theory and prove the concept on collected experimental data

Simulation

- build modular and reusable codebase in Python 3 that simulates the dynamics of quantized vortices using the *Vortex Filament* model
- implement stable time-step methods and a reliable re-segmentation process that allows keeping a good resolution of quantized vortices in different situations
- simulate a real-time quantum vortex ring motion and compare its properties and evolution in time with the theoretical approaches, thus validating the new codebase

1. Theoretical Background

The theoretical part of this Thesis is composed of two chapters:

1. Micro/Meso-scopic view - provides a theoretical cover of Gross-Pitaevskii model, creation and numerical modelling of the quantized vortex and its dynamics.
3. Macroscopic view - provides a hydrodynamics description of two-fluid model, oscillatory motion in He-II, creation of quantum turbulence, dynamical and universal scaling principles

The aim of the theoretical part is to introduce the basic properties of quantized vortex lines in Helium-II and summarize the state of art of current knowledge on superfluid turbulence. We also discuss the theoretical methods used to study quantized vorticity, quantum turbulence and the results obtained using such methods.

Micro/Meso-scopic view

One of the most useful ways of describing superfluid ^4He at $T = 0\text{ K}$ starts with non-linear Schrodinger equation (NLSE) for the one-particle wave function ψ . Since the superfluid ^4He is a strongly correlated system dominated by collective effects, this imperfect Bose-Einstein condensate (BEC) is approximately described by Gross-Pitaevskii equation (1.1). Although, it must be noted that the real Helium-II is a dense fluid, not a weakly interacting Bose gas described by NLSE.

1.1 Gross-Pitaevskii model

In terms of single-particle wavefunction $\psi(\mathbf{r}, t)$ we write the Gross-Pitaevskii model:

$$i\hbar \frac{\partial \psi}{\partial t} = -\frac{\hbar^2}{2m} \nabla^2 \psi + \psi \int |\psi(\mathbf{r}', t)|^2 V(|\mathbf{r} - \mathbf{r}'|) d\mathbf{r}', \quad (1.1)$$

where $V(|\mathbf{r} - \mathbf{r}'|)$ is the potential of two-body interaction between bosons. The normalization is set as $\int |\psi|^2 d\mathbf{r} = N$, where N is number of bosons. By replacing potential with repulsive δ -function of strength V_0 one obtains:

$$i\hbar \frac{\partial \Psi}{\partial t} = -\frac{\hbar^2}{2m} \nabla^2 \Psi - m\varepsilon \Psi + V_0 |\Psi|^2 \Psi, \quad (1.2)$$

where ε is the energy per unit mass and $\Psi = A e^{i\Phi}$ is a macroscopic wave function of condensate. In this way one can define the condensate's density $\rho_{BEC} = m\Psi\Psi^* = mA^2$ and velocity $\mathbf{v}_{BEC} = (\hbar/m)\nabla\Psi$. Note that equation (1.2) is equivalent to a continuity equation and an modified Euler equation (by the so called quantum pressure term).

Hereafter we identify ρ_{BEC} with ^4He superfluid component's ρ_s at absolute zero and \mathbf{v}_{BEC} with \mathbf{v}_s . It must be noted that this identification is convenient from the point of view of having a simple hydrodynamics model but is not entirely correct. The reason is that Helium-II is a dense fluid, not the weakly interacting Bose gas described by the NLSE (1.1), so the condensate is not the same as the superfluid component.

Even though the superfluid is irrotational: $\omega = \nabla \times \mathbf{v}_s = \mathbf{0}$, the NLSE has a vortex-like solution: $\mathbf{v}_s = \boldsymbol{\kappa}/2\pi r \mathbf{e}_\theta$, where θ is the azimuthal angle and $\boldsymbol{\kappa} = 9.97 \times 10^{-4} \text{ cm}^2 \cdot \text{s}^{-1}$ is the *quantum of circulation*, obtained from:

$$\boldsymbol{\kappa} = \oint_{\mathcal{C}} \mathbf{v}_{BEC} \cdot d\ell = \frac{\hbar}{m}, \quad (1.3)$$

where \mathcal{C} is a closed loop surrounding the vortex core - a topological defect (**Figure 1.1**) within macroscopic wavefunction Ψ

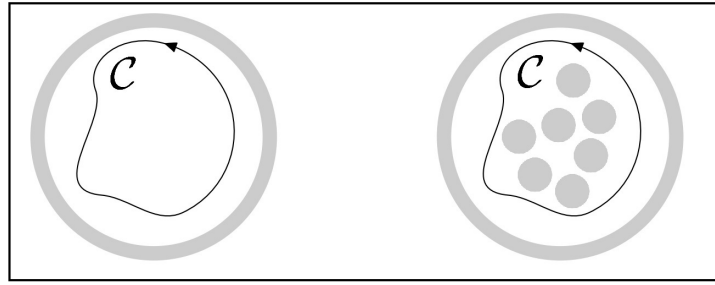


Figure 1.1: An illustration of topological singularities within a superfluid ${}^4\text{He}$. Left: A singly-connected region with circulation along \mathcal{C} loop equal to zero. Right: A multiply-connected region with depicted cores of quantized vortices with a finite circulation along \mathcal{C} loop.

1.2 Quantized vortex

As Feynman showed [6], superfluid vortex lines appear when Helium-II moves faster than a certain critical velocity. The simplest way to create quantum vortices is to rotate cylinder with superfluid Helium-II with high enough angular velocity Ω . Created vortex lines form an ordered array of density $L = 2\Omega/\boldsymbol{\kappa}$, all aligned along the axis of rotation (**Figure 1.2**). *Vortex line density* L can be also interpreted as a total vortex length in an unit volume.

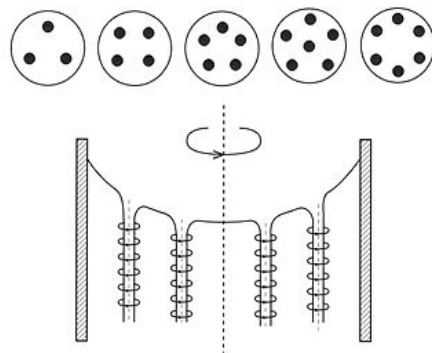


Figure 1.2: Array of quantized vortices in a rotating container

The key properties of Onsager-Feynman vortex [7] are the quantized circulation \varkappa , superfluid rotational velocity field $\mathbf{v}_s = \varkappa/2\pi r \mathbf{e}_\theta$ and the *vortex core parameter* a_0 . The core size a_0 can be estimated by substituting \mathbf{v}_s back into (1.2) and solving differential equation for ρ_s . One finds that ρ_s tends to the value $m^2\varepsilon/V_0$ for $r \rightarrow \infty$ and to zero density for $r \rightarrow 0$. The characteristic distance over which Ψ collapses (superfluid density ρ_s drops from bulk value to zero) is $a_0 \approx 10^{-10} \text{ m} = 1 \text{ \AA}$. From this, there is a conclusion that the vortex is hollow at its core and therefore, a topological defect occurs.

Taking a_0 as core radius, the energy considerations showed that a single vortex containing N circulation quanta owns more energy than N singly-quantized vortices. Hence it is generally assumed that only ground-state vortices are commonly observed.

Clearly, vortex lines don't have to be aligned in general. In most cases, the superfluid flow is strongly chaotic, better known as *quantum turbulence*. This topic is covered in more detail later in this work.

1.3 Vortex filament model

The vortex line can be represented as a curve via position vector $\mathbf{s} = \mathbf{s}(\xi, t)$ in three-dimensional space. Here, ξ is arclength along the vortex line. Next we label \mathbf{s}' as $d\mathbf{s}/d\xi$ and \mathbf{s}'' as $d\mathbf{s}'/d\xi$. Within our context, \mathbf{s}' is a tangent vector and $|\mathbf{s}''|$ is a local curvature R^{-1} at a given point. The triad of vectors $\mathbf{s}', \mathbf{s}'', \mathbf{s}' \times \mathbf{s}''$ are perpendicular to each other (**Figure 1.3**) and point along the tangent, normal and binormal respectively:

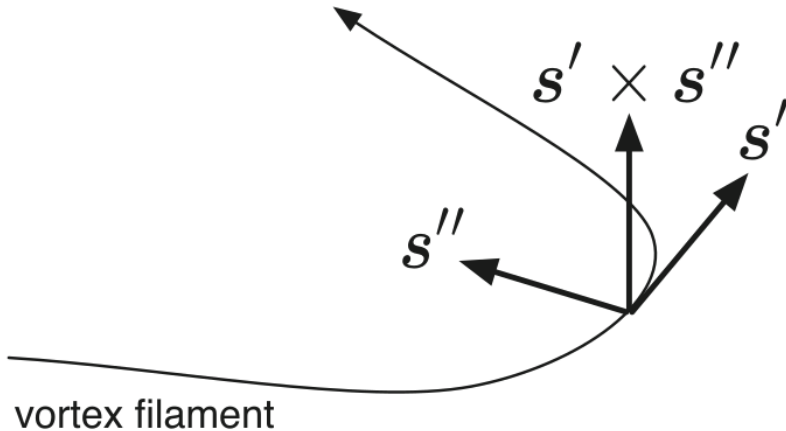


Figure 1.3: Schematic of the vortex filament and the triad vectors $\mathbf{s}', \mathbf{s}'', \mathbf{s}' \times \mathbf{s}''$. Source: [23]

We suppose that the superfluid component is incompressible $\nabla \cdot \mathbf{v}_s = 0$. Moreover, superfluid vorticity ω_s is localized only at positions of vortex filament $\omega_s(\mathbf{r}, t) = \nabla \times \mathbf{v}_s$.

Combining these two properties gives the Poisson equation $\Delta\phi = \omega_s$ for the potential ϕ . Using Fourier transform one obtains [26] the Biot-Savart law for the superfluid velocity:

$$\mathbf{v}_s(\mathbf{r}) = \frac{\kappa}{4\pi} \int_{\mathcal{L}} \frac{(\mathbf{r}' - \mathbf{r}) \times d\mathbf{r}'}{|\mathbf{r}' - \mathbf{r}|^3}, \quad (1.4)$$

where the integral path \mathcal{L} represents curves along all vortex filaments.

This law determines the superfluid velocity field $\mathbf{v}_s(\mathbf{r})$ via the arrangement of the vortex filaments. Now we define the *self-induced* velocity \mathbf{v}_{ind} , describing the motion which a vortex line induces onto itself ($\mathbf{r} \rightarrow \mathbf{s}$ in (1.4)) due to its own curvatures:

$$\mathbf{v}_{\text{ind}}(\mathbf{s}) = \frac{\kappa}{4\pi} \int_{\mathcal{L}} \frac{(\mathbf{r}' - \mathbf{s}) \times d\mathbf{r}'}{|\mathbf{r}' - \mathbf{s}|^3} \quad (1.5)$$

However, this integral (1.5) diverges as $\mathbf{r}' \rightarrow \mathbf{s}$ because the core structure of the quantized vortex was initially neglected. We avoid this divergence by splitting the integral into two parts - direct neighbourhood of the point \mathbf{s} (local part) and the rest \mathcal{L}' (nonlocal part). The Taylor expansion of the local part leads [22] to a finite result:

$$\mathbf{v}_{\text{ind}}(\mathbf{s}) = \mathbf{v}_{\text{ind,local}} + \mathbf{v}_{\text{ind,nonlocal}} \approx \beta \mathbf{s}' \times \mathbf{s}'' + \frac{\kappa}{4\pi} \int_{\mathcal{L}'} \frac{(\mathbf{r}' - \mathbf{s}) \times d\mathbf{r}'}{|\mathbf{r}' - \mathbf{s}|^3}, \quad (1.6)$$

$$\text{where } \beta = \frac{\kappa}{4\pi} \ln(R/a_0), \quad (1.7)$$

where \mathcal{L}' is the original vortex line without a close area of the studied vortex point and R is a *local curvature* and often is calculated as $1/|\mathbf{s}''|$ [22].

Since the local part of induced velocity (1.6) is a dominant term (and also computationally faster), the nonlocal part can be neglected. Such approximation process is called as *Local Induction Approximation* (LIA). LIA represents the contribution of local curvature to the induced velocity, whereas nonlocal Biot-Savart part represents the global filament curvature.

Since in the system there could be present also external flow sources of superfluid component (e.g. heat resistors causing *counterflows*), we define the total superfluid velocity $\mathbf{v}_{s,tot}$, in a laboratory frame, as:

$$\mathbf{v}_{s,tot} = \mathbf{v}_{s,ext} + \mathbf{v}_{\text{ind}} \quad (1.8)$$

1.4 Vortex dynamics

To determine the equation of motion of $\mathbf{s}(t)$ we recognize the forces acting upon the line - the magnus force \mathbf{f}_M and (at non-zero temperature $T > 0$ K) the drag force \mathbf{f}_D (both are per unit length).

The magnus force \mathbf{f}_M always arises when a rotating body moves in a flow. This causes a pressure difference, which in our case of moving vortex line with circulation quantum \varkappa , exerts a force:

$$\mathbf{f}_M = \rho_s \varkappa \mathbf{s}' \times (\dot{\mathbf{s}} - \mathbf{v}_{s,tot}), \quad (1.9)$$

where $\dot{\mathbf{s}} = d\mathbf{s}/dt$ is the velocity of a particular point on a vortex line.

The drag force \mathbf{f}_D arises from the *mutual friction*, the interaction between the normal component and vortex lines (quantized superfluid component). According to the findings of Vinen and Hall [8], the normal fluid flowing with velocity \mathbf{v}_n past a vortex core exerts a frictional force \mathbf{f}_D on the vortex line, given by:

$$\mathbf{f}_D = -\alpha(T) \rho_s \varkappa \mathbf{s}' \times [\mathbf{s}' \times (\mathbf{v}_{ns} - \mathbf{v}_{ind})] \quad (1.10)$$

$$-\alpha'(T) \rho_s \varkappa \mathbf{s}' \times (\mathbf{v}_{ns} - \mathbf{v}_{ind}), \quad (1.11)$$

where $\mathbf{v}_{ns} = \mathbf{v}_n - \mathbf{v}_{s,ext}$ is the difference between the average velocity of normal component and the applied superfluid velocity.

The temperature dependent dimensionless parameters $\alpha(T)$ and $\alpha'(T)$ are often written in terms of measured *mutual friction parameters* B and B' , which are known from experiments by Samuels and Donnelly [9]:

$$\alpha(T) = \frac{\rho_n B(T)}{2\rho} \quad \alpha'(T) = \frac{\rho_n B'(T)}{2\rho} \quad (1.12)$$

The precise calculation of the mutual friction parameters $B(T), B'(T)$ over the entire temperature range is still an open problem. Although, we already know that in the area of high temperatures, the friction arises mainly from the scattering processes of rotons.

Since the mass of vortex core is usually neglected, the two forces \mathbf{f}_M and \mathbf{f}_D add up to zero: $\mathbf{f}_M + \mathbf{f}_D = \mathbf{0}$. Hence, solving for $d\mathbf{s}/dt$, we obtain [22] the Schwarz's equation:

$$\dot{\mathbf{s}} = \mathbf{v}_{s, \text{ext}} + \mathbf{v}_{\text{ind}} + \alpha \mathbf{s}' \times (\mathbf{v}_{ns} - \mathbf{v}_{\text{ind}}) - \alpha' \mathbf{s}' \times [\mathbf{s}' \times (\mathbf{v}_{ns} - \mathbf{v}_{\text{ind}})], \quad (1.13)$$

On the basis of Schwarz's equation (1.13), algorithms to numerically simulate vortex time evolution of an arbitrary configuration can be developed. Also, the vortex parametrisation $\mathbf{s}(\xi, t)$ and dynamics description provide the baseline of what we call as Vortex Filament (VF) model. More on VF model is written later in **Simulation** chapter.

Quantized vortex rings

A special case of vortex line configuration are a freely moving vortex rings. Such rings are usually created as a result of multi-vortex interconnections [5] or by the self-reconnection of an oscillating loop pinned to the surface of a vibrating body. The exact expressions derived from the Gross-Pitaevskii equation (1.1) [10] for the energy E and induced center velocity v_{ind} of a vortex ring, moving in a Helium-II of density ρ and having a radius R much greater than its core radius $R \gg a_0$, are:

$$E = \frac{1}{2} \kappa^2 \rho R \left(\ln(8R/a_0) - 2 + c \right) \quad (1.14)$$

$$v_{\text{ind}} = \frac{\kappa}{4\pi R} \left(\ln(8R/a_0) - 1 + c \right), \quad (1.15)$$

where c is a constant based on inner structure of the vortex. Since we work with hollow core, we use [11] $c = 1/2$. Note that (1.14) and (1.15) depend on a_0 only logarithmically. The behavior of the vortex ring is thus quite insensitive to the exact value of a_0 (expected to be of the order of atomic dimension).

Relations (1.14) and (1.15) are derived directly from Gross-Pitaevskii description and no dissipative process (mutual friction) was included. Therefore, the relations hold only for temperature $T = 0$ K. Using the explicit dynamical equation [11] for vortex ring motion, one can also derive the final ring center velocity \mathbf{v}_{ring} and energy E_{ring} using (1.14) and (1.15) like:

$$\mathbf{v}_{\text{ring}} = (1 - \alpha')(\mathbf{v}_{\text{ind}} - \mathbf{v}_{s, \text{ext}}) + \alpha' \mathbf{v}_{n, \text{ext}} \quad (1.16)$$

$$E_{\text{ring}} = \left(\frac{\alpha}{1 - \alpha'} \right) E \quad (1.17)$$

Several other interesting results come from the ring's dynamic motion equation and the mutual friction formula (1.10), (1.11). The second term (1.11) of friction force causes the decrease of vortex ring radius, whereas the first term (1.10) is the dissipative term. The superfluid vortex ring (**Figure (1.4)**) living in a mixture of a normal and superfluid component has therefore a limited lifetime expectancy and the travelled distance.

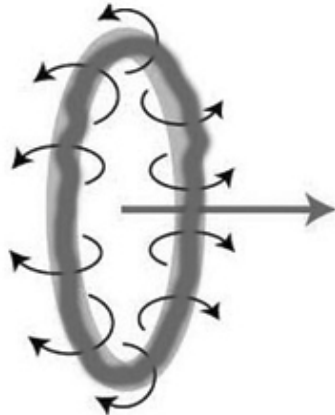


Figure 1.4: Depiction of quantized vortex ring motion and induced velocity field. Source: Huang, Kerson, *Quantum vorticity in nature*, arXiv.

More explicitly, it was shown [11] that in case of weak counterflow velocity \mathbf{v}_{ns} , the lifetime of vortex ring can be expressed as a simple relation:

$$\tau_{\text{ring}} = \frac{R_0}{2\alpha|\mathbf{v}_{\text{ring}}(R_0)|}, \quad (1.18)$$

where R_0 is the initial radius of created vortex ring.

By integrating the ring's motion equation from R_0 to $R(\tau) \approx a_0$ we obtain the distance travelled by the ring's center:

$$D_{\text{ring}} = \frac{\alpha}{1 - \alpha'} (R_0 - a_0) \quad (1.19)$$

Relations (1.18) and (1.19) are taken as a baseline in **Simulation** chapter.

Macroscopic view

Besides NLSE and Vortex filament model, there is also a third, *macroscopic* model in which the individual vortex lines are *invisible* and the superfluid component of Helium-II is considered as a continuous flow of vortices. Many phenomena are similar to those in classical hydrodynamics (**Figure 1.5**), but there emerge also new and very special type of events that can happen within superfluid Helium-II.

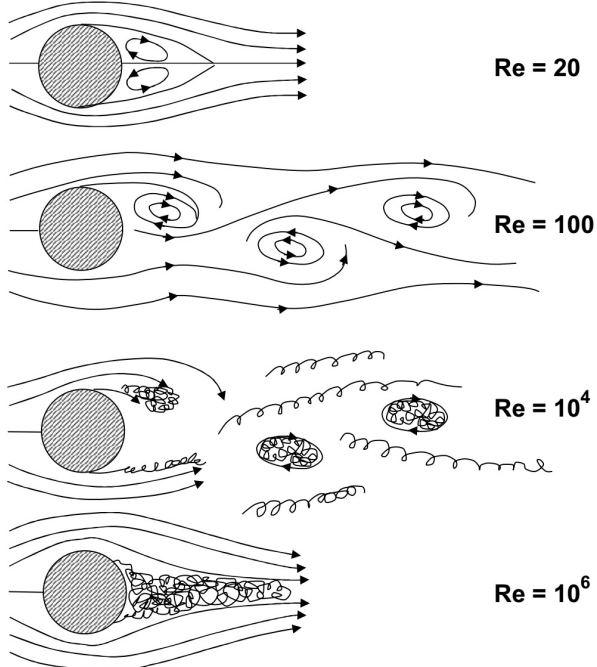


Figure 1.5: Depiction of a classical steady flow for various Reynolds number values. Many phenomena of laminar, semi-turbulent and turbulent flows are visible in depcitions. Source: [13]

1.5 Hydrodynamics of superfluid

Such macroscopic model is called the Hall-Vinen-Bekarevich-Khalatnikov (HVBK) model and provides a generalization of Landau's two-fluid model equations, including the presence of vortices. The superfluid is treated as a continuum and we can define a macroscopic superfluid vorticity Ω_s , despite the fact that, microscopically, the superfluid velocity field obeys $\nabla \times \mathbf{v}_s = \mathbf{0}$. The downside of this model is its assumption of spatially (not randomly) organized vortices. The common example is a rotating cylinder [12].

The incompressible HVBK equations for normal component $\mathbf{v}_n(\mathbf{r}, t)$ and superfluid component $\mathbf{v}_s(\mathbf{r}, t)$, respectively, are [26]:

$$\frac{\partial \mathbf{v}_n}{\partial t} + (\mathbf{v}_n \cdot \nabla) \mathbf{v}_n = -\frac{1}{\rho} \nabla P - \frac{\rho_s}{\rho_n} S \nabla T + \frac{\eta}{\rho_n} \nabla^2 \mathbf{v}_n + \mathbf{F}_{ns}, \quad (1.20)$$

$$\frac{\partial \mathbf{v}_s}{\partial t} + (\mathbf{v}_s \cdot \nabla) \mathbf{v}_s = -\frac{1}{\rho} \nabla P + S \nabla T + \mathbf{T} - \frac{\rho_n}{\rho} \mathbf{F}_{ns}, \quad (1.21)$$

where we have defined:

$$\mathbf{F}_{ns} = \frac{B(T)}{2} \hat{\boldsymbol{\Omega}} \times [\hat{\boldsymbol{\Omega}}_s \times (\mathbf{v}_n - \mathbf{v}_s - \nu_s \nabla \times \hat{\boldsymbol{\Omega}})] + \frac{B'(T)}{2} \boldsymbol{\Omega}_s \times (\mathbf{v}_n - \mathbf{v}_s - \nu_s \nabla \times \hat{\boldsymbol{\Omega}}_s), \quad (1.22)$$

$$\boldsymbol{\Omega}_s = \nabla \times \mathbf{v}_s, \quad (1.23)$$

$$\hat{\boldsymbol{\Omega}}_s = \boldsymbol{\Omega}_s / |\boldsymbol{\Omega}_s|, \quad (1.24)$$

$$\mathbf{T} = -\frac{\kappa}{4\pi} \log(b_0/a_0) \boldsymbol{\Omega}_s \times (\nabla \times \hat{\boldsymbol{\Omega}}_s) \quad (1.25)$$

Here we can identify the quantities as \mathbf{F}_{ns} (mutual friction force), \mathbf{T} (vortex tension) and η (viscosity parameter). Usually, b_0 is the intervortex spacing and can be estimated as $b_0 = (2\Omega_s \kappa)^{-1/2}$. The HVBK equations have well-defined limiting cases:

- $T \rightarrow T_\lambda$: In this case $\rho_s \rightarrow 0$ and the normal fluid motion equation (1.20) becomes the classical Navier-Stokes equation with viscosity term.
- $T \rightarrow 0$: In this case $\rho_n \rightarrow 0$ and the superfluid motion equation (1.21) describes a pure (potential) superflow. Additionally, taking the classical limit ($\hbar \rightarrow 0$) would give us the pure Euler equation of inviscid fluid.

The HVBK model has been widely used with success to study the transition to classical or quantum turbulence, for estimations of critical Reynolds numbers and its temperature dependence.

1.6 Dynamical similarity principle

An important role in the behaviour of fluids is taken by the *fluid dimensional numbers*, which are used for scaling of motion equations in fluid mechanics.

The principle of *dynamical similarity* states that two flows of similar geometry have the same dynamical behaviour, if they can be characterised by the same set of suitable dimensionless parameters representing transport phenomena. In order to describe Helium-II with correct equations and with the most precision, we have to choose which dimensionless parameters are useful.

- Knudsen number (Kn): This number helps determine whether statistical mechanics or the continuum mechanics formulation of fluid should be used to model the system. Kn is defined as the ratio of the molecular mean free path λ to a representative physical length scale D (container size).

If the temperature of Helium-II is set above $T > 1.0\text{ K}$, there is a still sufficient amount of normal component and the mean free path of thermal excitations is much smaller, comparing it with container scale $\lambda \ll D$. In that case, continuum mechanics could be used as a macroscopic theory for superfluid Helium-II.

However, if temperature is below $T < 0.6\text{ K}$, the mean free path λ becomes comparable with length scale D and the continuum model starts to break down. Here, the system is rather described as a gas of thermal excitations.

- Weissenberg number (Wi): This number relates the typical frequency of perturbations, ω , of the fluid with the characteristic time, τ that describes the relaxation of the fluid towards a thermodynamic equilibrium. The Weissenberg number is then given as a multiplication of oscillation frequency ω and the relaxation time τ .

Since the relaxation time of Helium-II is relatively small in temperatures above $T > 1\text{ K}$, then $\text{Wi} = \omega\tau \ll 1$, so Helium-II can be considered as a Newtonian fluid.

Once again, if temperature is below $T < 0.6\text{ K}$, relaxation time of thermal excitations rises rapidly, meaning $\text{Wi} \sim 1$, causing the excitations propagating ballistically.

- Reynolds number (Re): Let's consider the continuum and newtonian assumptions ($\text{Kn} \ll 1$ and $\text{Wi} \ll 1$), so the fluid can be described by the raw form of Navier-Stokes (N-S) equation of motion. When we take into account also the incompressibility $\nabla \cdot \mathbf{v} = 0$, the N-S for classical fluid reduces itself to its most simplest form. In case of stationary flow ($\partial \mathbf{v} / \partial t = 0$), N-S can be rewritten into a dimensionless form. Following these steps, there arises typical values of velocity U and length

scale L , at which there is the most significant change in velocity. Re can be expressed as a ratio of inertial and dissipative forces as $\text{Re} = UL\rho/\eta$, where η is the dynamic viscosity of the flow field.

The oscillatory case is described more in the next section.

The derivation of the *dynamical similarity* phenomenon can be directly seen from inspection of the underlying motion equation (1.20) with geometrically similar bodies. In the classical fluid dynamics, we use dynamical similarity and scaling arguments for expressing experimental data in terms of Reynolds numbers, drag coefficients, lift, and so on.

Alternatively, the dissipative forces may be described in terms of a dimensionless *drag coefficient* C_D , representing the relation between *drag force* \mathbf{F} and fluid velocity \mathbf{U} , and usually takes the form:

$$C_D \propto U^\alpha, \quad \text{where } \begin{cases} \alpha = -1 & \text{for laminar flow } \text{Re} \in (0 - 10) \\ \alpha = 0 & \text{for turbulent flow } \text{Re} \in (10^3 - 10^5) \end{cases},$$

where the first case ($C_D \propto 1/U$) represents the viscous skin friction and the second case ($C_D \approx \text{const.}$) represents the pressure drag.

It is very common to plot experimentally measured dependence of drag coefficient C_D against the Reynolds number, for various objects (sphere, disc, cylinder) past flow:

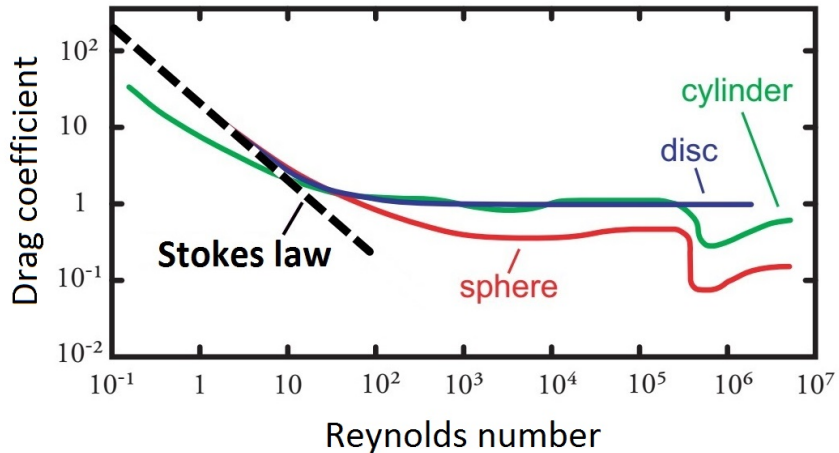


Figure 1.6: Drag coefficients of different objects in a steady flow with changing Reynolds number. Blue line - thin disc, Green line - cylinder with drag crisis near $\text{Re} \approx 10^6$, Red line - sphere with similar drag crisis as with cylinder, Black dashed line - laminar drag, where $C_D \propto \text{Re}^{-1}$.

Dynamical similarity argument also leads to the existence of critical Reynolds number, at which the transition to turbulence in case of classical fluid occurs. Note that since superfluid Helium-II is composed of two fluids, the mentioned applies only to the normal

component. The transition of superfluid component to quantum turbulence is described wider in next chapters

1.7 Oscillatory flows

If a given body is oscillating in a classical viscous fluid, described by ordinary Navier-Stokes equation, there appears another characteristic lenght scale, identified by [2] as the *viscous penetration depth*:

$$\delta(\omega) = \sqrt{\frac{2\eta}{\rho\omega}}, \quad (1.26)$$

where ω is the angular frequency of oscilations.

To recognize correct characteristic length scale (whether it should be oscillating body dimension D or penetration depth δ), we calculate the ratio of time-dependent term $\partial\mathbf{v}/\partial t$ from N-S equation (1.20) to the viscous term $\nabla^2\mathbf{v}$. Hence, we define another dimensionless quantity, the Stokes number β . We calculate it [14] as $\beta = \omega\rho D^2/(\pi\eta)$, which can be reduced using (1.26) to $\beta = D^2/(\pi\delta^2)$.

From this, we call a situation as the *high-frequency regime*, when $\delta \ll D$, so the Stokes values are $\beta \gg 1$.

Classical hydrodynamics

To describe fully an oscillatory flow, the governing Navier-Stokes equations may be expressed in terms of dimensionless velocity U , time T and positions L . The independent time scale is given by the angular frequency of oscillations ω . Candidates for characteristic lenght scale L may lead to the body size D , surface roughness, or the viscous penetration depth $\delta(\omega)$.

In the high frequency limit (directly from 1.26) $\omega \gg 2\eta/(\rho D^2)$, depending on body geometry, one can reach $\delta(\omega) \ll D$ and say that fluid oscillates in high Stokes regime [4] with $\beta = D^2/(\pi\delta^2) \gg 1$. Also, when also the surface roughness exceeds δ , the N-S equation may be expressed using only one dimensionless parameter: an *oscillatory Reynolds number* $\text{Re}_\delta = \delta U \rho / \eta$.

Superfluid Helium-II

Assuming two independent velocity fields $\mathbf{v}_n(\mathbf{r}, t)$, $\mathbf{v}_s(\mathbf{r}, t)$ in superfluid Helium-II, the above thoughts are applicable for the oscillatory viscous flow of the normal component \mathbf{v}_n . We therefore define the high frequency limit for normal component as:

$$\delta_n = \sqrt{\frac{2\eta}{\rho_n\omega}}, \quad Dn = \frac{U\delta_n\rho_n}{\eta}, \quad (1.27)$$

We will call the oscillatory Reynolds number for normal component in superfluid Helium-II as a *Donnelly number* (Dn , after Russell J. Donnelly, who as first came with this (1.27) idea).

At low velocities, below the critical thresholds to create either classical or quantum turbulence, the flow of the superfluid component is purely potential and the normal component exhibits laminar viscous flow.

If the typical body curvature is of order $1/D$, the surface may be described as if consisting of many planar elements. In this case it is shown [4] that we can write for the average dissipated energy:

$$\langle \dot{E} \rangle = \frac{1}{2}\alpha\xi U_0^2 S_{eff} \sqrt{\frac{\eta\rho_n\omega}{2}}, \quad (1.28)$$

where U_0 is the velocity amplitude, S_{eff} the effective surface, α the mutual friction constant and ξ the integral of velocity profile along the resonator. The total energy of an oscillator is given as $E = \xi m U_0^2 / 2$ and moreover, we define a fluidic quality factor Q_f of an oscillator for a single oscillation as:

$$1/Q_f = \frac{\langle \dot{E} \rangle}{\omega E} = \frac{\alpha\rho_n S_{eff} \delta_n}{2m} \quad (1.29)$$

From (1.28), one can also derive the peak dissipative force (during a period of oscillation) and the dimensionless drag coefficient related to the normal component:

$$F_0 = \frac{2\omega \langle \dot{E} \rangle}{U_0} = \alpha\xi\omega S_{eff} U_0 \sqrt{\frac{\eta\rho_n\omega}{2}} \quad \rightarrow \quad C_D^n = \frac{2F}{A\rho_n U_0^2} = \frac{2S_{eff}}{AU_0} \sqrt{\frac{\eta\omega}{\rho_n}}, \quad (1.30)$$

where A is the cross-section of the body perpendicular to flow. According to dynamical similarity principle, the drag coefficient (1.30) can be expressed as a function of the

dimensionless Donnelly number (1.27):

$$C_D^n = \Phi / D_n , \quad (1.31)$$

where number Φ is determined by the oscillating body geometry. Clearly, the laminar case of normal component is fully described by the hydrodynamic laws. In turbulent case, we expect a constant value for C_D^n as long, as only normal component contributes to the drag force (no quantum turbulence).

1.8 Quantum turbulence

Turbulence of superfluid component can be viewed as a tangle of vortex lines. In this case quantized vortices can be nucleated either *intrinsically* (such process requires critical velocities of order 10 m/s) or *extrinsically*, by stretching and reconnections of seed vortex loops. The initial vortices in the extrinsical case are the remnant vortices, which always exist in macroscopic samples of Helium-II . In many types of flow the critical velocity for extrinsic vortex nucleation is observed to be in order \sim cm/s.

The superfluid component becomes turbulent at some critical velocity U_C and therefore, we expect an increase in drag coefficient C_D much above the possible dependence caused by turbulence of normal component. The process of self-reconnecting remnant vortices was well studied [4] and the related critical velocity is expected to scale as $U_C \propto \sqrt{\varkappa\omega}$, where \varkappa is the circulation quantum. Hence, it is convenient to define a dimensionless velocity \hat{U} with related drag coefficient C_D^s as:

$$\hat{U} = U_0 / \sqrt{\varkappa\omega} \quad \rightarrow \quad C_D^s = \frac{2F_0}{A\rho_s U_0^2} = \frac{2F_0}{A\rho_s \varkappa\omega \hat{U}^2} , \quad (1.32)$$

In case of turbulent superfluid component with velocities sufficiently above critical values, we expect both component to be coupled due to the mutual friction. In this case, both components contribute to the pressure drag, and drag coefficient must be calculated classically as $C_D = 2F/(A\rho U^2)$. where ρ is the total density of Helium-II.

Ultra-low temperature regime

In classical fluids, when the mean free path λ of particles becomes comparable to a length scale D of the system ($\text{Kn} \sim 1$), the continuum model of the fluid starts to break down and the system cannot longer be described by the Navier-Stokes equations. Similar arguments go when the angular frequency of oscillatory flow ω becomes comparable with the relaxation time τ of the fluid towards thermodynamic equilibrium ($\text{Wi} = \omega\tau \sim 1$). Here, the system is described as a gas of thermal quasiparticles propagating ballistically through a physical vacuum. Therefore, such system state is called as *ballistic regime*.

In practice with superfluid Helium-II, such situation is usually reached by cooling fluid down to ultra-low temperatures. Below $T < 1\text{ K}$, the normal component accounts for less than 1% of the total density, but required cooling to obtain ballistic regime (**Figure (1.7)**) is below $T < 0.6\text{ K}$ (here the Helium-II is better described as a gas of thermal quasiparticles than a fluid).

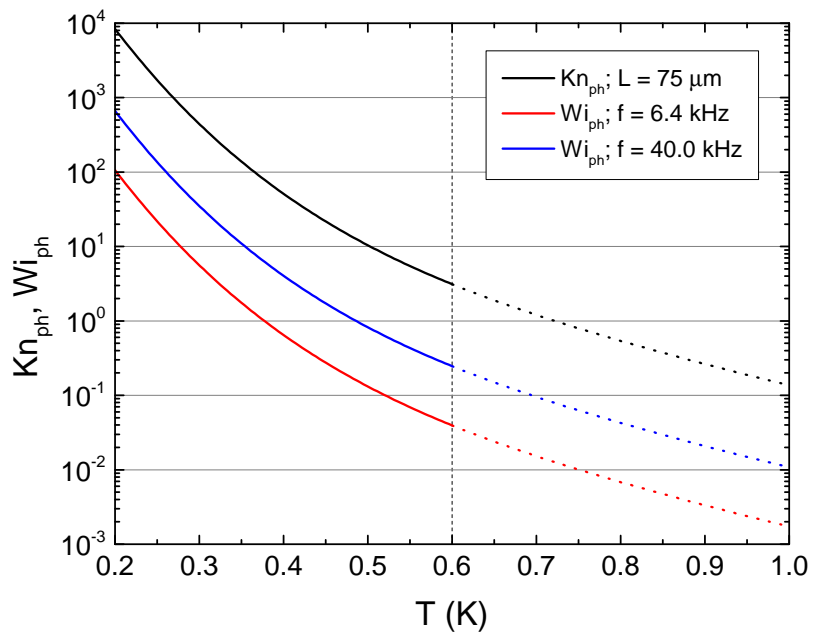


Figure 1.7: Phonon Knudsen number and Weissenberg numbers plotted against temperature for different oscillators. The dashed line separates the interval $T < 0.6\text{ K}$, where the ballistic regime takes a place. Source: [4]

Universal scaling

A study was conducted in order to solve the Stokes' second problem with an oscillating plane in viscous fluid, using pure Boltzmann kinetic equation. This solution is used to derive a universality relation valid in the high frequency limit (with no turbulence present) across both Newtonian and non-Newtonian regimes of the fluid. Using scaling function $f(\omega\tau)$, the authors derived [4] the relation for the quality factor:

$$1/Q_f = \frac{\alpha S_{eff}}{m} \sqrt{\frac{\eta \rho_n}{2\omega}} f(\text{Wi}) \quad (1.33)$$

In **Results** we use this form of universality scaling for comparison against experimental data collected in temperature ranges $T < 0.6$ K or $T > 1$ K.

Multiple critical velocities

Here is briefly commented the transition to quantum turbulence regime observed at very low temperatures ($T \ll 1$ K). A couple of experimental studies in milliKelvin temperatures reported [15] the existence of more critical velocities related with superfluid component flow within single experiment:

- First critical velocity is related to the formation of pinned vortex loops at the surface of oscillating body - possibly forming a thin layer with different hydrodynamic behaviour which increases the effective mass of the oscillating object. Such critical velocity is hard to observe at higher than ultra-low temperatures.
- Second critical velocity is a consequence of vortex rings escaping from the oscillator body into the superfluid bulk and eventually forming a vortex tangle. Here the sudden raise of drag is observed, usually with hysteresis effect.
- Third critical velocity is the highest critical velocity which can be observed. The origin of this velocity is linked to the development of larger quantized vortex structures, which in larger scale start to mimic the classical turbulence. Such velocity is in order \approx m/s and moreover, very likely screened by the influence of the normal component turbulence. Therefore, not likely reachable within experiments reported in this Rhesis.

2. Experimental Approach

Experiments presented in this Thesis were conducted in Prague, with members of department of low-temperature physics, under Charles University.

Many experimental methods were conducted in order to launch the production of quantum turbulence: by an oscillating objects (wires, the tuning forks, oscillating discs, etc.) or by *coflow* and *counterflow* techniques (in other words, using indirect flow sources).

In our investigation, we used the tuning fork oscillator, driven by alternating source Agilent A33220 and measured by SR830 amplifying lock-in, using an I/V converter with an conversion ratio 1000 V/A [16]. We measured both the in-phase and anti-phase componentes of signals. Measurements with other oscillators are included and analysed in this Thesis, but the experimental work was not performed by the Thesis' author.

2.1 Apparatus

All the measurements were performed in a helium cryostat, cooled down to the desired temperatures using a rotary and Roots pump, and stabilized (with errors of a few mK) either manually or using a Lake Shore temperature controller Model 340. The most of used technologies are captured in a photograph **Figure 2.1**.

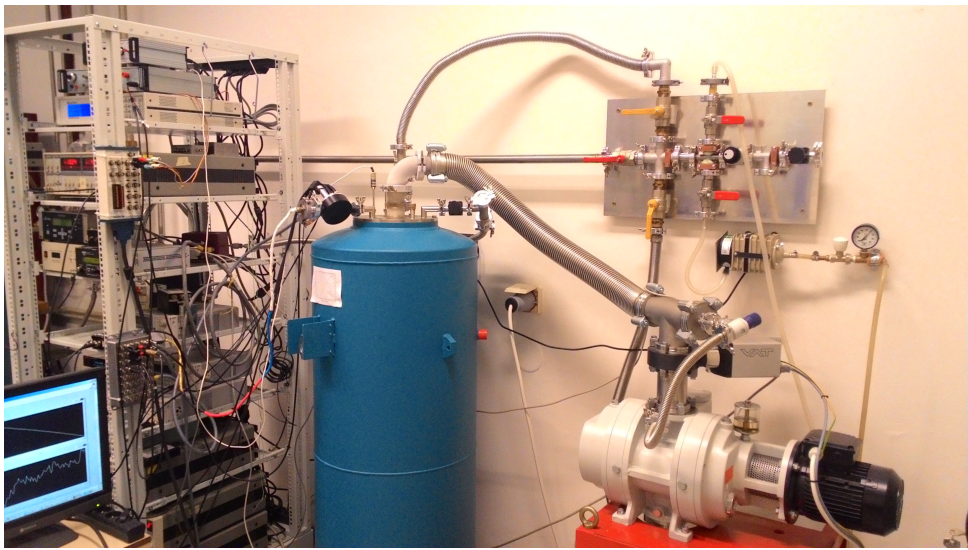


Figure 2.1: A photograph of the experimental setup. From left: source generators, lock-in, cryostat, gas handling system for emerging gas, Roots pump. Source: [21]

The working temperatures are from a wide range from a little above T_λ to the lowest (experimentally) possible one $T_{\min} \approx 1.3\text{ K}$. We also added series of measurements from area far above T_λ , when $T = 3\text{ K}$ to compare our results with a fully classical fluid in hydrodynamic regime.

The range ($1.3\text{ K} - 2.17\text{ K}$) allows access to the most ratios of the two-fluid regime ($\rho_s/\rho_n \ll 1$ at $T \sim 2.17\text{ K}$ and $\rho_s/\rho_n \approx 20$ at $T \sim 1.30\text{ K}$).

Measurements at temperatures $T < 0.6\text{ K}$ in the ballistic regime were performed on a Leiden Cryogenics MNK126-400 dilution refrigerator with a base temperature below 10 mK . The description of sub-Kelvin measurements is not included in this Thesis, but are discussed in sufficient detail in the attached manuscript [4]. However, refrigerator results are analysed in **Results** part to test the *uniform scaling* theory, introduced in **Theoretical part**.

A *second-sound resonator* housing the tuning fork oscillator was attached at the bottom (**Figure 2.2**) of the *insert* - a large metallic construction holding all measuring micro-devices.

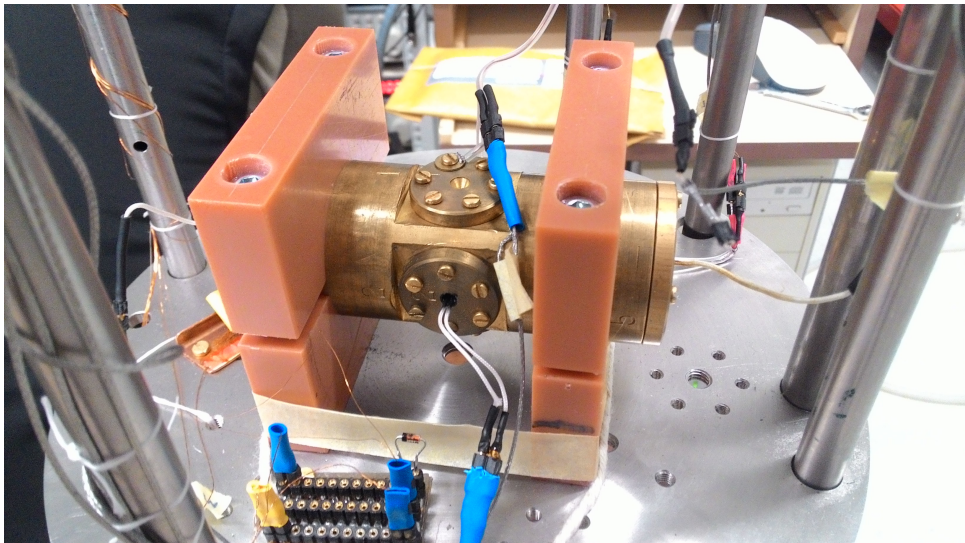


Figure 2.2: A photograph of the second-sound resonator attached at the bottom of metallic insert. Source: [21]

To obtain the best results at low temperatures in superfluid helium, the cryostat containing oscillators was repeatedly flushed with pure liquid ^4He from Dewar transport container. After this pre-cooling step, the liquid ^4He was transferred using a siphon.

The inner space of resonator was separated from the outer part (cryostat body) by a sintered copper, forming a solid mass of material by pressure. This ensures that no parasitic helium ices microparticles or other impurities will interfere with the oscillators inside of resonator.

2.2 Resonators

In this section we briefly describe the principles of micro-scale oscillators used in experiments with Helium-II.

Vibrating Wire

Vibrating wire resonator consists of a semi-circular loop of wire inserted to a vertical magnetic field \mathbf{B} , as shown in **Figure 2.3**. As we turn on the alternating current flux $\mathbf{j} \propto e^{i\omega t}$ inside the wire, these currents forces the wire to oscillate due to Lorentz force $\mathbf{F}_L \propto \mathbf{j} \times \mathbf{B}$. As the wire moves through the field, the Faraday voltage is induced of magnitude [17]:

$$V = -\frac{d(\mathbf{B} \cdot \mathbf{S})}{dt} \sim \frac{\pi}{4} B D U, \quad (2.1)$$

where \mathbf{S} is the area vector, enclosed by the wire loop and D is the distance between wire's legs. Experimentally used magnetic field was about ≈ 170 mT with an uncertainty of ± 10 mT.

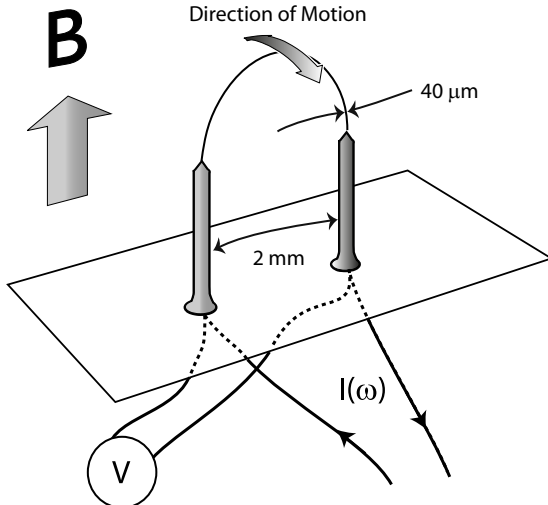


Figure 2.3: Schematic diagram of the vibrating wire resonator. Source: [4]

Tuning Fork

Quartz tuning forks (TF) are commercial piezoelectric oscillators with a well-calibrated resonant frequency. They are usually used as frequency standards in watches or as force sensors in microscopes. Also, TFs have started to be widely used in cryogenic Helium II experiments [18].

In our experimental setup, we used the fork of following dimensions: prongs length $\mathcal{L} = 3.50\text{ mm}$, prongs width (perpendicular to the fork plane) $\mathcal{W} = 75\mu\text{m}$, thickness $\mathcal{T} = 90\mu\text{m}$ prongs interdistance $\mathcal{D} = 90\mu\text{m}$. The same type of fork was also used and discussed in [19] [20] A sketch of the fork architecture is depicted in **Figure 2.4**:

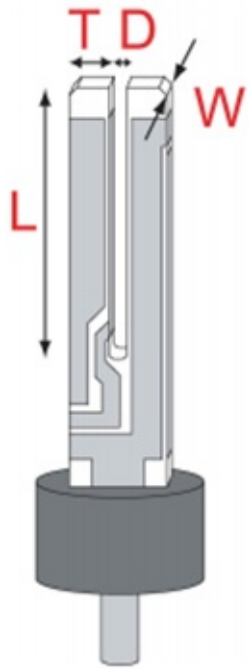


Figure 2.4: Schematic diagram of the quartz tuning fork. Source: [21]

There are several achievable resonant modes at which the fork can oscillate. We chose to work with the *fundamental* one at $f_0 = 6.7\text{ kHz}$ and with the first *overtone* one at $f_1 = 41\text{ kHz}$.

The fork is driven by applying an alternating voltage $V(t) \propto e^{i\omega t}$ from a generator to the metallic plates (deposited on fork surface). The piezoelectric effect causes a tension resulting in a force, which is proportional to the applied voltage. In fundamental mode, the fork exhibits an anti-phase oscillating motion of its prongs with a single node. In case of overtone, there would be just two nodes. The fork's flexion induces a piezoelectric current $I(t)$ which is proportional to the velocity $U(t)$.

The conversion relations between applied $V(t)$, measured $I(t)$ and mechanical properties $F(t)$, $U(t)$ are given [18] as:

$$F(t) = \frac{1}{2}a_f V(t), \quad U(t) = \frac{I(t)}{a_f}, \quad (2.2)$$

where a_f is the so-called *fork constant*. This constant can be derived from a fork's geometry, material and an oscillation mode. Usually the formula for this constant is given by a deflection measurement:

$$a_f = \sqrt{4\pi m_{eff} \Delta f \frac{I}{V}}, \quad (2.3)$$

where $m_{eff} = TWL\rho_q/4$ (ρ_q as the quartz density) is the fork's effective mass and Δf is the measured peak width from the frequency-sweep deflection measurement. In our case we used fork with the effective mass and fork constants for fundamental and overtone mode of following values:

$$m_{eff} = 1.52 \times 10^{-8} \text{ kg}, \quad a_{f0} = 0.30 \times 10^{-8} \text{ Cm}^{-1}, \quad a_{f1} = 1.41 \times 10^{-8} \text{ Cm}^{-1} \quad (2.4)$$

The measurement scheme of the experiment with tuning fork is shown in **Figure 2.5**. The arrangement of experiments using dilution refrigerator were slightly more complex and are described in [16].

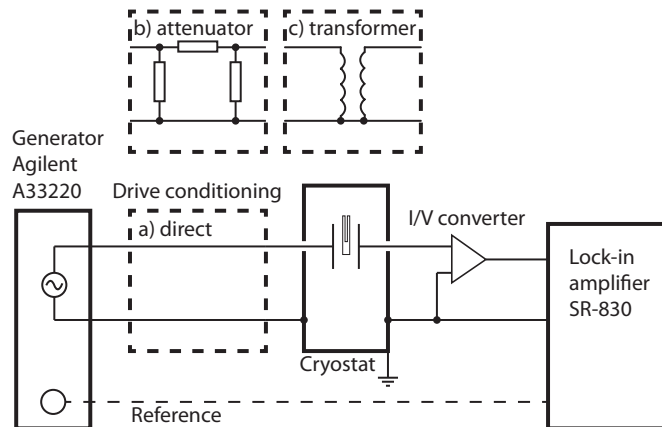


Figure 2.5: Diagram of the measurement scheme used in Prague. To achieve the full range of velocities, the applied voltage was either (a) directly fed to the tuning fork, (b) attenuated by one or more inline attenuators, or (c) amplified by a transformer. The transformer's output was constantly monitored by a Keithley digital multimeter Model 2100. Source: [20]

Oscillating Disc

The torsional oscillator consists of a $50\mu\text{m}$ wire with a glass disc fixed to the wire at its midpoint. The disc is 1 mm thick with a diameter of 40 mm. A schematic picture is showed in **Figure 2.6**.

Sixteen black marks around the circumference of the disc are used to determine the deflection and angular velocity of the disc from recorded video sequences.

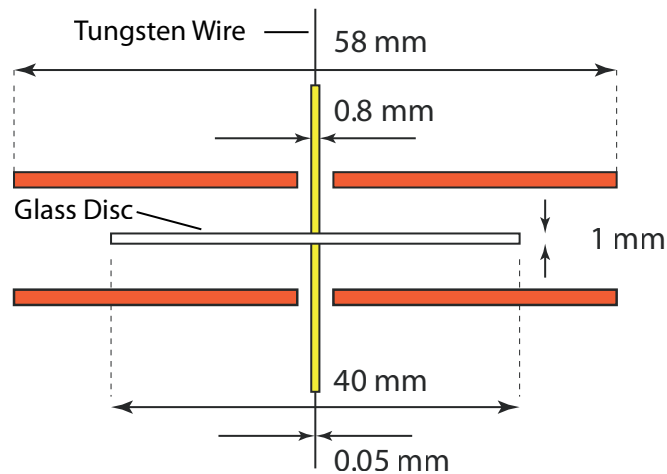


Figure 2.6: Schematic diagram of the torsionally oscillating disc. Source: [4]

The raw data is in the form of video recordings of the disc motion and fairly complex post-processing method was required to extract quantities. The optical distortion from the lenses and the curved walls of the cryostat are negligible. More details about data processing can be found in [4].

3. Simulations

This part of Thesis serves as a general description of the **PyVort** codebase, a new platform to simulate quantum vortices. The code is written in well commented **Python 3**, arranged in a modular structure. The primary aim of this chapter is to highlight which modules are involved and how they work. On GitHub, one can find a table of the parameters (user's options) which can be set in the `config.py` file to run the simulation.

At present, we use infinite boundary conditions. Therefore, only closed-loop vortices can be realized in simulation. However, the codebase is flexible and supports the potential implementation of unclosed loops.

3.1 Vortex filament model

The **PyVort** code is based on vortex filament (VF) model, a technique pioneered by Schwarz [22] in the early 1980s. Superfluid vortex filament is represented by a series of mesh points (segments) distributed along the centerline of the filament (**Figure 3.1**). The motion of the whole VF is summed up by the motion of each mesh point.

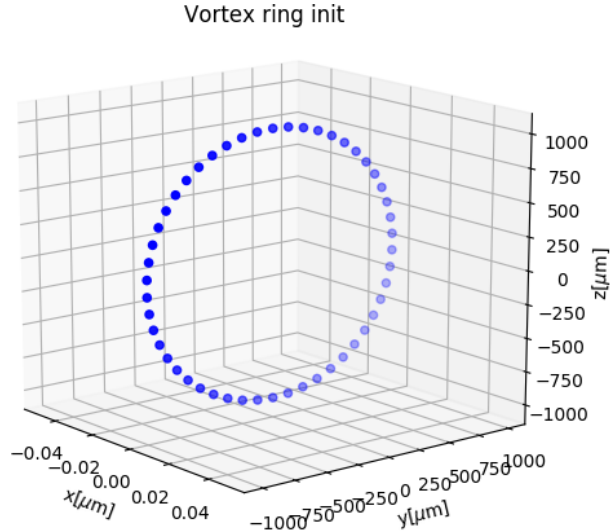


Figure 3.1: Visualisation of vortex ring segments right after their initialisation.

As introduced in **Theoretical Background** chapter, we define the VF more precisely as a three dimensional curve $\mathbf{s}(\xi, t)$, where ξ represent an arc-lengths and t the time. Each segment, indexed as (i) (i is increasing as we move along the VF) is localised by its assigned coordinates \mathbf{s}_i and direct neighbours indices: *previous* $(i - 1)$ and *next* $(i + 1)$.

This leads to a data structure called as *directed digraph*, which is the array structure we implemented.

Next we define the tangent vector \mathbf{s}' , then normal vector \mathbf{s}'' , and the binormal vector $\mathbf{s}' \times \mathbf{s}''$, as depicted in **Figure 1.3**, by taking numerical derivatives. Note $\mathbf{s}' = d\mathbf{s}/d\xi$ and $\mathbf{s}'' = d\mathbf{s}'/d\xi$. Numerical derivatives are achieved using *Finite Differences* method, as introduced in next subsection.

Finite differences

In order to properly calculate the numerical derivatives \mathbf{s}' and \mathbf{s}'' , belonging to the directed 3D curve, we need to use a sophisticated numerical method. At a particular segment (i) with position \mathbf{s}_i , we define the distance to the particle in-front \mathbf{s}_{i+1} as $l_i = |\mathbf{s}_{i+1} - \mathbf{s}_i|$ and the distance to the particle behind \mathbf{s}_{i-1} as $l_{i-1} = |\mathbf{s}_i - \mathbf{s}_{i-1}|$ (**Figure 3.2**). By in-front/behind we refer to the particles next/previous along the filament.

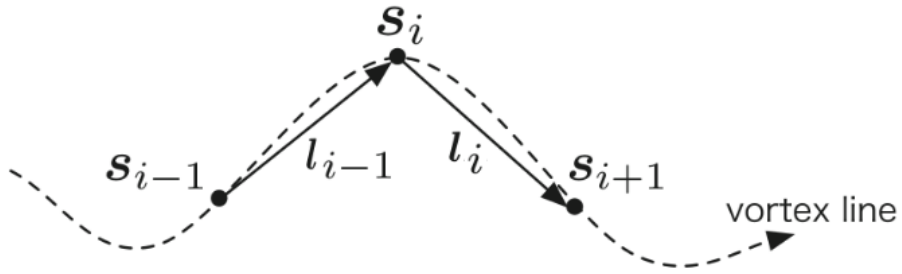


Figure 3.2: Depiction of i -th segment vector and its corresponding lengths. Source: [23]

For accuracy, we approximate all the spatial derivatives \mathbf{s}'_i , \mathbf{s}''_i by a fourth-order finite difference method (FD), which can also account the varying distances along the vortex filament. With this, the first and second derivatives can be obtained based on coordinates of 2 closest neighbours (on each side).

Using FD theorem, we can construct the approximations by taking the Taylor's series expansions. We can then write:

$$\frac{d^n \mathbf{s}_i}{d\xi^n} \approx A_i \mathbf{s}_{i-2} + B_i \mathbf{s}_{i-1} + C_i \mathbf{s}_i + D_i \mathbf{s}_{i+1} + E_i \mathbf{s}_{i+2} \quad \text{for } n \in \{1, 2\} \quad (3.1)$$

Calculation of coefficients A, B, C, D, E can be done using analytical solution of *Vandermonde matrix* inversion. This inversion can be done also numerically, which is a more scalable way of implementation, however, this method often meets with problems when the Vandermonde matrix becomes singular. In code, there is implemented both the an-

alytical solution (closed form) and the solution by inverting the Vandermonde matrix. The closed form works for exactly our form of approximation (3.1) and is more described in [24], whereas the numerical method works generally for any approximation level.

Biot-Savart discretisation

We denote the dynamic external sources of velocity fields (which can be set in `config.py`) as $\mathbf{v}_{n,ext}(\mathbf{r}, t)$ and $\mathbf{v}_{s,ext}(\mathbf{r}, t)$. The equation of motion for a given segment is then given directly by Schwarz's equation(1.13):

$$\frac{d\mathbf{s}_i}{dt} = \mathbf{v}_{s,ext} + \mathbf{v}_{\text{ind}}^{(i)} + \mathbf{v}_{\text{drive}}^{(i)} \quad (3.2)$$

The first difficulty in the VF model comes from the calculation of term \mathbf{v}_{ind} . As we shown previously in (1.6), this advection term can be split into the LIA part and a Biot-Savart integral:

$$\mathbf{v}_{\text{ind}}^{(i)} = \mathbf{v}_{\text{LIA}}^{(i)} + \mathbf{v}_{\text{BIOT}}^{(i)} = \frac{\kappa}{4\pi} (\mathbf{s}'_i \times \mathbf{s}''_i) \ln \left(\frac{2\sqrt{l_{i-1}l_i}}{a} \right) \quad (3.3)$$

$$+ \frac{\kappa}{4\pi} \int_{\mathcal{L}'} \frac{(\mathbf{r}' - \mathbf{s}_i) \times d\mathbf{r}'}{|\mathbf{r}' - \mathbf{s}_i|^3}, \quad (3.4)$$

where l_{i-1} and l_i are the arc lengths of the curve between points \mathbf{s}_{i-1} and \mathbf{s}_i and between \mathbf{s}_i and \mathbf{s}_{i+1} respectively, and \mathcal{L}' is the original vortex line without the two segment lines between \mathbf{s}_{i-1} and \mathbf{s}_{i+1} .

Using the segment discretisation, the Biot-Savart integral can be rewritten [25] into the sum of single-line contributions (**Figure 3.3**) between each j -th and $j + 1$ -th segment (except for the ones attached to the i -th point):

$$\mathbf{v}_{\text{BIOT}}^{(i)} \approx \frac{\kappa}{4\pi} \sum_{j \notin \{i-1, i\}} \frac{(R_j + R_{j+1})(\mathbf{R}_j \times \mathbf{R}_{j+1})}{R_j R_{j+1} (R_j R_{j+1} + \mathbf{R}_j \cdot \mathbf{R}_{j+1})}, \quad (3.5)$$

where $\mathbf{R}_j = \mathbf{s}_j - \mathbf{s}_i$ and $\mathbf{R}_{j+1} = \mathbf{s}_{j+1} - \mathbf{s}_i$ are the relative vectors from the given point.

Note that, if one takes in account the Biot-Savart law for N mesh points, the computational time is proportional to $\mathcal{O}(N^2)$, while, if one uses just the LIA term, it is only $\mathcal{O}(N)$. Numerical simulations based on Biot-Savart are therefore significantly more com-

putationally expensive, even with the speed of today's computers.

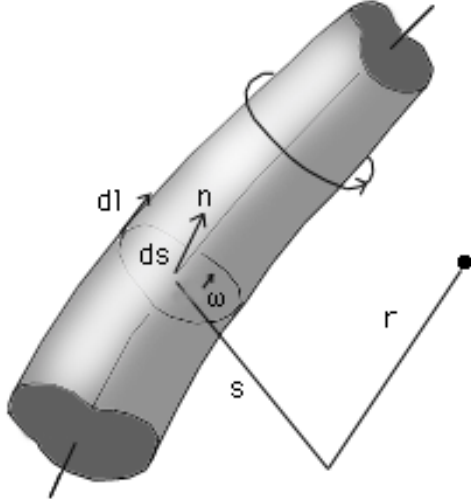


Figure 3.3: An infinitesimal contribution of a j -th segment line between two points \mathbf{s}_j and \mathbf{s}_{j+1} at a given point \mathbf{r} . Source: Internet

One way to get around this difficulty is to update the LIA term. In this method we neglect completely the non-local Biot-Savart integral and keep just the local term. This is typically done with a minor adjustments within the log term:

$$\mathbf{v}_{\text{LIA}}^{*(i)} = \frac{\kappa}{4\pi} (\mathbf{s}'_i \times \mathbf{s}''_i) \ln \left(\frac{2R_i}{a} \right), \quad (3.6)$$

where R_i is a i -th segment local length scale - may be taken [26] as a local curvature: $R_i = 1/|\mathbf{s}''_i|$. Updated LIA approach (3.6) is a very convenient approximation and works very well for calculating the motion of a single vortex ring.

3.2 Implementation

In code, a system consisting of flow sources and a single vortex ring object is represented using several `class` structures. These structures are updated after each time step. We will call them as a *state* of the system and it is defined (and initialised) with following properties:

Environment class

- external normal component - defines an external source of normal component flow
- external normal component - defines an external source of superfluid component flow

Ring class

This class is initialized only when the purpose of simulation is to collect physical and statistical data about vortex rings.

- center - an array of ring center coordinates
- radius - current radius of the ring object
- direction - a normal vector pointing in a direction toward which the ring is moving
- velocity - measured velocity of the ring center

Vortex class

- number of active segments - number of active segments N the vortex ring is composed of
- segments - an array of all segments, each one with following attributes:
 - activity - a logical value whether a particular segment should be considered as a part of vortex object
 - coordinates - an array of segment coordinates $\mathbf{s}_i = [x_i, y_i, z_i]$
 - previous/next neighbour - array localisation indices of the *previous* ($i-1$) and the *next* ($i+1$) segment within the context of the directed vortex
 - tangent/curvature - a tangential and normal vectors \mathbf{s}'_i and \mathbf{s}''_i
 - LIA velocity - a self-induced velocity $\mathbf{v}_{\text{LIA}}^{(i)}$ driven by the local curvature.
 - BIOT velocity - a self-induced velocity driven by the farther segment lines of the vortex ring $\mathbf{v}_{\text{BIOT}}^{(i)}$
 - Drive velocity - a velocity given by the mutual friction force $\mathbf{v}_{\text{drive}}^{(i)}$
 - Full velocity - the sum of external sources $\mathbf{v}_{s,\text{ext}}$, LIA velocity $\mathbf{v}_{\text{LIA}}^{(i)}$, BIOT velocity $\mathbf{v}_{\text{BIOT}}^{(i)}$ and the drive velocity $\mathbf{v}_{\text{drive}}^{(i)}$, resulting in $d\mathbf{s}_i/dt$

All functions that are manipulating with segments' attributes are implemented as Vortex class methods. Before each time stepping, all attributes has to be updated and tested. We used numerical methods already introduced in previous section and tests that are described in next section.

Initialisation

The proper initialisation of the *state* in the very beginning of simulation requires several physical inputs. This is done in following steps:

0. Symbolically, we expect as a *0-th step* the environmental setup of the system - *external sources, temperature, time-step,....*
1. If interested in quantized ring simulation, we expect several ring inputs from user: *center, radius, direction* and *resolution*. Resolution parameter is the initial desired distance δ between each two neighbouring segments. This set of 4 inputs makes an unambiguous ring object, ready for next updates.
2. After creation, we initialise neighbour indices (to an i -th element in segment array will be assigned $i - 1$ index as the *previous* and $i + 1$ index as the *next* neighbour index)
3. Next we calculate all s' and s'' using Finite differences method
4. Final step is the calculation of all segment velocities using motion equations and their approximative forms.

After these four steps, we obtain a fully updated ring object that can be propagated in time.

3.3 Time evolution

Now after we defined and ran all the necessary calculations leading to the quantum vortex ring's *state* fulfillment, we can start to propagate it in time.

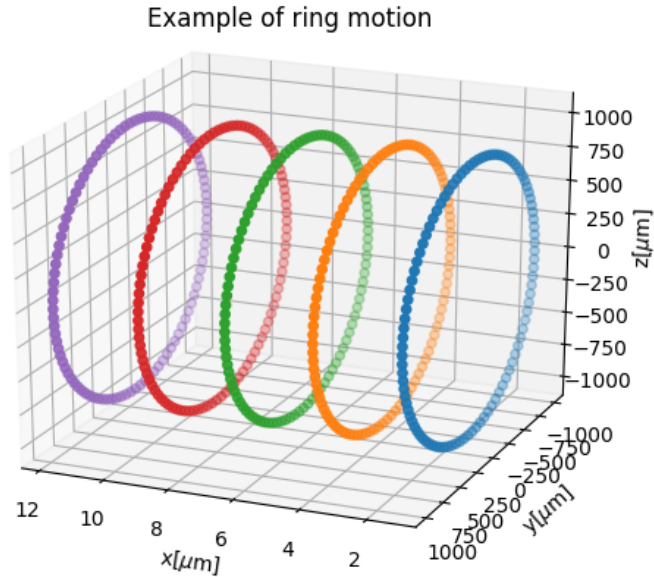


Figure 3.4: Example of a moving vortex ring

Time stepping

Time evolution is based on an explicit iterative method: the fourth-order Runge-Kutta (RK4) scheme. When we consider the Schwarz's equation $d\mathbf{s}_i/dt \equiv \mathbf{v}_{\text{full}}^{(i)}$, the stepping algorithm is given as:

$$\mathbf{s}_i(t + dt) = \mathbf{s}_i(t) + \frac{dt}{6}(\mathbf{v}_1^{(i)} + 2\mathbf{v}_2^{(i)} + 2\mathbf{v}_3^{(i)} + \mathbf{v}_4^{(i)}), \quad (3.7)$$

where dt is the time step and the velocities $\mathbf{v}_1^{(i)}, \mathbf{v}_2^{(i)}, \mathbf{v}_3^{(i)}, \mathbf{v}_4^{(i)}$ are the induced velocities of partial steps:

$$\mathbf{v}_1^{(i)} = \mathbf{v}_{\text{full}}^{(i)}(\mathbf{s}_i, t), \quad (3.8)$$

$$\mathbf{v}_2^{(i)} = \mathbf{v}_{\text{full}}^{(i)}(\mathbf{s}_i + \mathbf{v}_1^{(i)} dt/2, t + dt/2), \quad (3.9)$$

$$\mathbf{v}_3^{(i)} = \mathbf{v}_{\text{full}}^{(i)}(\mathbf{s}_i + \mathbf{v}_2^{(i)} dt/2, t + dt/2), \quad (3.10)$$

$$\mathbf{v}_4^{(i)} = \mathbf{v}_{\text{full}}^{(i)}(\mathbf{s}_i + \mathbf{v}_3^{(i)} dt, t + dt) \quad (3.11)$$

Lower-order schemes such as basic Euler method is also implemented in code, however, not recommended to use. More on this is discussed in Results part of thesis.

The time step dt is adaptively changing so that the vortex ring cannot move faster than a 1% of its size in a single step. As we will see later in Results, in case of vortex rings with changing radius, the time step dt has to be iteratively changing after each break of the above rule:

$$dt \leftarrow \frac{0.01R}{|\mathbf{v}_c|} \quad (3.12)$$

3.4 Re-segmentation of vortex

To obtain the most realistic simulation (to catch effects on any length scale), the natural tendency would be to set the resolution parameter δ as low as possible. However, the CPU time cost rises rapidly as the number of segments N increases, so there is need to find the best trade-off.

As the distance between neighbouring segments is compressed/enlarged with time due to the physics and numerical inaccuracies, there is need for remove/add segments (*re-segment*) in order to conserve the vortex resolution δ . The closeness (in terms of arclength) of neighbouring segments is therefore measured after each simulation time-step.

We used the simplest re-segmenting criteria - keeping an approximately *uniform distance* between the segments. To ensure this, two boundary conditions were implemented:

1. The segment \mathbf{s}_{j+1} would be removed if:

$$|\mathbf{s}_{j+1} - \mathbf{s}_j| < \delta_{\min}, \quad (3.13)$$

where δ_{\min} is the minimal distance between two segments. Also, the segment \mathbf{s}_j would take place somewhere between \mathbf{s}_{j-1} and \mathbf{s}_{j+2} so that it will conserve the

curvature of vortex. Such result can be obtained using any spline interpolation along nearest neighbours. We worked with 3D local spline using 4 points (in our context they would be \mathbf{s}_{j-2} , \mathbf{s}_{j-1} , \mathbf{s}_{j+1} , \mathbf{s}_{j+2}) and create another 11 interpolated knots. Consequently, the new position of \mathbf{s}_j will sit on the 6-th (the middle one) knot and also.

2. In a similar manner, we add a new segment \mathbf{s}_{new} between \mathbf{s}_j and \mathbf{s}_{j+1} if:

$$|\mathbf{s}_{j+1} - \mathbf{s}_j| > \delta_{\max}, \quad (3.14)$$

where δ_{\max} is the maximal allowed distance between two segments.

This method keeps all the distances along the vortex roughly in the range $\delta \in \langle \delta_{\min}, \delta_{\max} \rangle$ and also keeps the geometrical properties.

Real-time tests

After each time step is done, a few tests are performed, to ensure that vortex itself is behaving according to our expectations. The tests are following:

- Length test - This test calculates the vortex circumference as $l = \sum_j |\mathbf{s}_j - \mathbf{s}_{j+1}|$ and compare it with the theoretical one $2\pi R$. If the deviation from the theoretical value is too high $> 1\%$, the segments are noisy and the process is killed. In case of deviation below $< -1\%$, there is clearly too less segments and resegmentation is called.
- Segmentation test - Here we check the value $l_j |\mathbf{s}_j - \mathbf{s}_{j+1}|$ for each j and ask whether $l_j \in \langle \delta_{\min}, \delta_{\max} \rangle$. If not, resegmentation is called.
- Smallness test - If the vortex ring radius would decrease below $R < \delta_{\min}$, the ring is deleted from the simulation.

3.5 Future implementations

To make Pyvort a full-fledged quantum vortex simulation, there should be implemented following improvements:

Complexity speedup

Recent numerical research presented [27] a new numerical method to compute the evolution of vortex filament. The method is based on an N-body cosmological simulation by Barnes and Hut [28], a *tree algorithm* which considerably speeds up the calculation of Biot-Savart integrals - computational cost scales as $\mathcal{O}(N \log(N))$ rather than N^2 . Properties of the tree method was tested for a variety of vortex configurations, ranging from simple vortex rings to a counterflow vortex tangle and compared with the LIA approach and the exact Biot-Savart's law.

Implementation of such algorithm is not easy, but definitely worth for the speed-up property.

Re-connection process

If any lines of two vortices (or even the single one) become very close, the filaments can reconnect, changing the topology of the system. Many researchers experimentally reported this is happening and also found analogies with vortex dynamics in the Navier–Stokes equation.

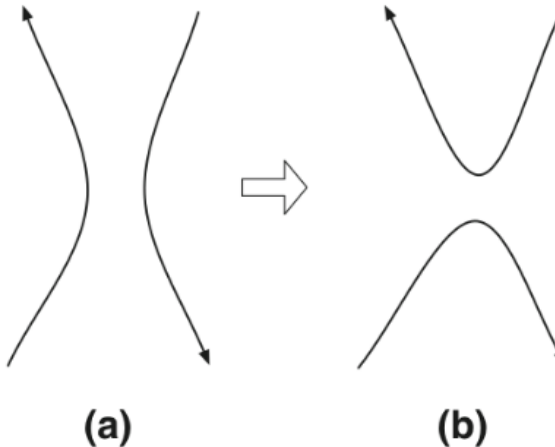


Figure 3.5: Reconnection of quantized vortices. (a) Two vortices before reconnection, about to contact each other. (b) The new vortices after reconnection.

The VF model itself cannot describe the reconnection process because the vortex core structure is neglected. Hence, some artificial procedures must be introduced to simulate such process. For instance, when two vortices approach within a critical distance δ_{\min} , we will artificially reconnect the vortices.

The main criteria for reconnection is that the total length (this is corresponding with

energy) will decrease. Self-reconnections (e.g. caused by a twist of vortex) would be treated in the same way. Since reconnection involves only antiparallel vortices, one has to check using the inner product whether two vortices could physically reconnect or not.

High-order tests

Once the code of interacting vortex filaments is developed, the analysis of all that data has to be improved. The simplest measurable quantity is the total length of all vortex lines. In a finite volume this would be $L = (1/V) \int d\xi$ for the vortex line per unit volume.

Of course, there can be defined more complicated metrics, measuring the isotropy of the vortex tangle. One of them is the length of line projected along a given vector $\hat{\mathbf{r}}$, give as:

$$J(\hat{\mathbf{r}}) = \frac{1}{VL} \int_{\mathcal{L}} \sqrt{1 - (\mathbf{s}'(\xi) \cdot \hat{\mathbf{r}})^2} d\xi \quad (3.15)$$

4. Results

In this chapter we present our investigations in numerical simulations using methods from **Simulations** chapter, and measurements from oscillatory experiments introduced in **Experimental Approach** chapter.

In the first part of this chapter, we analyse the functionality of new codebase. We made several tests on energy conservation, precision of numerical methods and stability, to ensure that simulation is reliable and stable for further development.

In the second part, we present our drag force measurements by using the oscillators. We start with the two-fluid regime (temperature above $T > 1.3\text{ K}$) and connect these results with those from ballistic regime ((temperature below $T < 0.6\text{ K}$)).

4.1 Simulation experiments

All presented measurements and results were done in order to setup the `config` file and thus to recommend the best simulation parameters for future investigations. We performed tests with physical motivation and also tests focused on precision and stability. With presented findings, there should be ensured the reliability and stability of any further high-scale simulation.

Zero-temperature test

In case of zero temperature $T = 0\text{ K}$, there should be no *normal component* in superfluid He-II and therefore also no mutual friction. In such case, velocity and energy of vortex ring is conserved due to the lack of energy dissipation processes.

We plotted in **Figure 4.1** the ring velocity $|\mathbf{v}_{\text{ring}}|$ and energy E_{ring} evolving in time, for the case of temperature $T = 0$ (pure superfluid, no normal component) and $T = 1.5\text{ K}$ (considerable ratio of present normal and superfluid component).

We tested the mutual friction effect during 1000 time-steps (calling *epochs*) with varying dt according to (3.12).

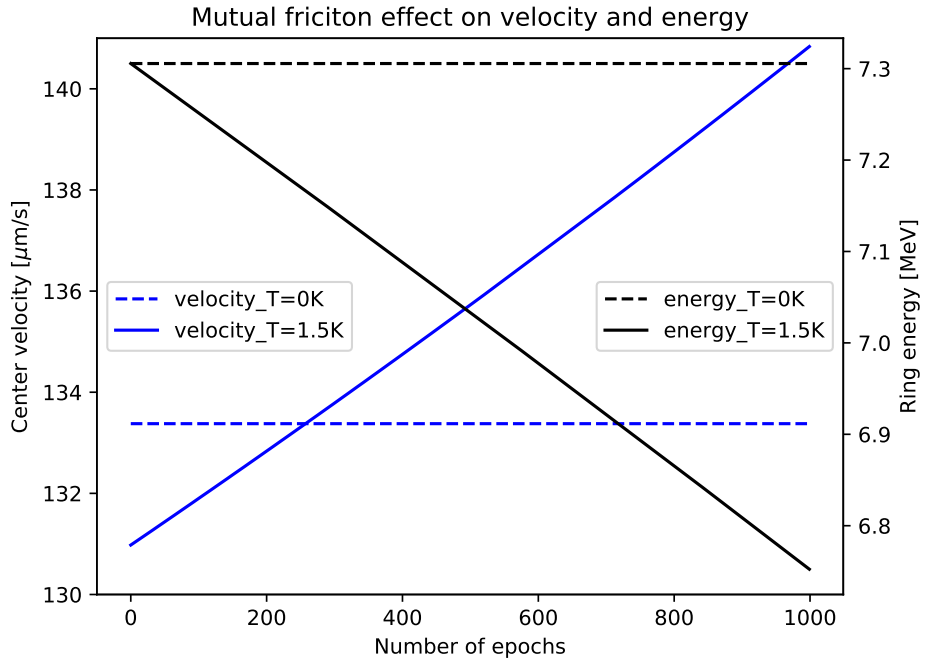


Figure 4.1: Evolution of ring velocity and energy in time. Blue lines - measured velocity data, Black lines - measured energy data, Dashed lines - the constant behaviour for temperature $T = 0\text{ K}$, Full lines - the dissipative process for temperature $T = 1.5\text{ K}$.

On x axis, we plot the number of elapsed epochs (time steps) and on y axis the velocity of the ring center $|\mathbf{v}_{\text{ring}}|$ and ring energy E_{ring} .

As we see, at $T = 0\text{ K}$ the velocity and energy is conserved even after 1000 epochs of simulation due to missing dissipation process (mutual friction). In case of $T = 1.5\text{ K}$, energy is falling down as expected, whereas the velocity is increasing. This increase is physically well-explained by the fact that the radius is decreasing with time due to the non-dissipative term of mutual friction. Also, the theoretical formula (1.15)

Velocity precision test

Our first velocity test compares the various approaches how can the ring velocity $|v_c|$ be calculated. Here, we recognize between four approaches, based on its theoretical motivation, computational complexity and precision:

- LIA (3.3): motivated [26], computationally cheap, not precise
- LIA + BIOT (3.3 + 3.4): motivated [26], but computationally expensive
- updated LIA (3.6): not well motivated [25], but computationally cheap and precise
- Theoretical (1.15): well motivated [10] and most precise

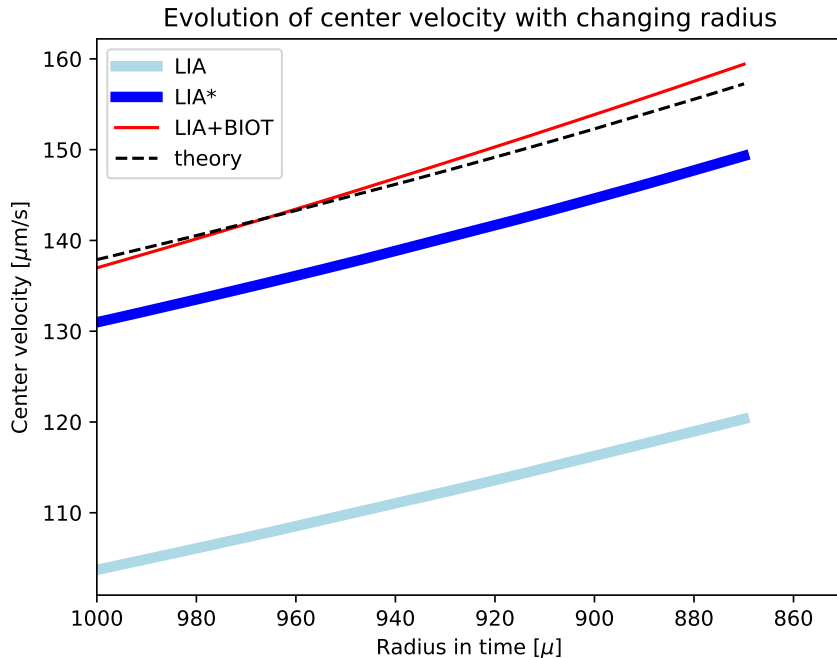


Figure 4.2: Comparison of all implemented velocity approaches (full lines) with the theoretical one (black dashed line) according to (1.15), with decreasing radius in time.

On x axis, we plot the number of elapsed epochs (time steps) and on y axis the ring velocity $|v_{ring}|$.

The theoretical values for velocity from (1.15) is taken as a baseline that other velocity calculations are compared with. All velocities were measured and evolved over a few thousands epochs (time steps), during which the radius was dissipatively decreasing, as is sketched in **Figure 4.2**.

We see that the theoretically most precise (LIA + BIOT) approach grows a bit faster than it should according to theory. This inconsistence is caused by bad resolution parameter,

which was set at $\delta \approx 70\mu\text{m}$

Therefore, for all further measurements we used the updated LIA velocity (LIA*) approach due to its time-scale consistency and computational speed.

Velocity convergence test

Next, we investigated the magnitude of the ring velocity $|\mathbf{v}_{\text{ring}}|$ for various resolutions $\delta \in \langle 50, 200 \rangle \mu\text{m}$, immediately after initialisation and then after 100 epochs. Ring radius was always set at $R = 1000\mu\text{m}$ (this is usual working radius [23] [24]), so the number of discretisation points along the vortex was given by R and δ as $N \approx 2\pi R/\delta \in \langle 30, 120 \rangle$.

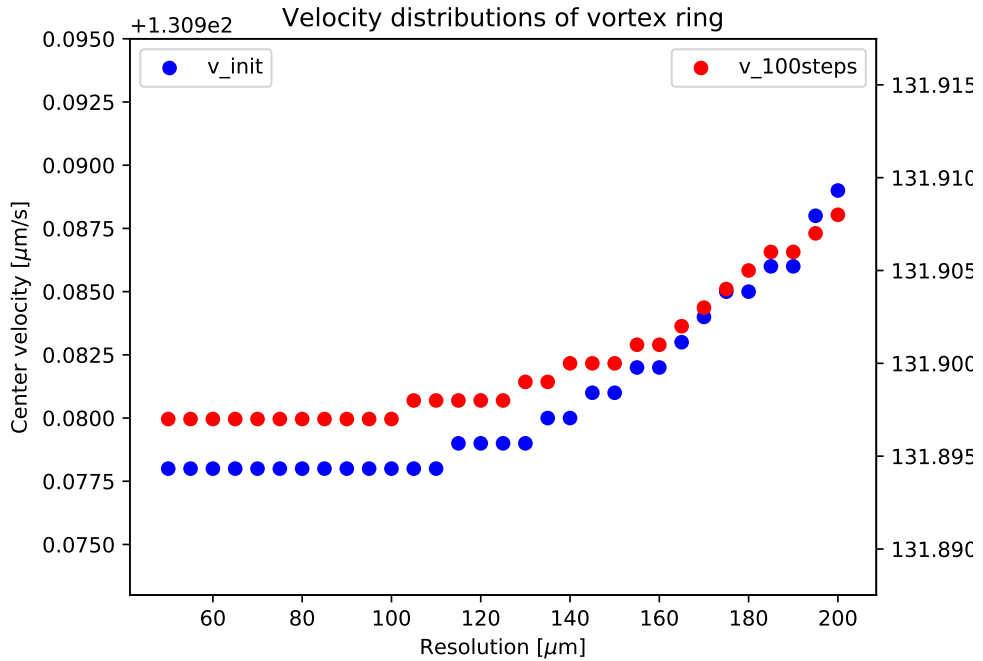


Figure 4.3: The distribution of ring velocity values $|\mathbf{v}_{\text{ring}}|$ for a range of resolution parameters δ in two situations. Blue dots - Velocity values immediately after initialisation, Red dots - velocity values after 100 time-steps.

On x axis, we plot the resolutions δ of vortex segments and on y axis the ring velocity $|\mathbf{v}_{\text{ring}}|$.

We see in **Figure 4.3** the expected convergent behaviour of both measured velocities in an area of good resolutions (small values of δ). It seems that below $\delta < 100\mu\text{m}$ (corresponding to ≈ 60 segments along the ring of radius $R = 1000\mu\text{m}$) the velocities perform enough convergent behaviour, which provides the upper boundary for a *good-chosen* resolution.

Even if it is intuitive that good resolutions (small δ -s) lead to more precise velocities, the high number of vortex segments $N \propto 1/\delta$ worsens the stability of simulation in time.

The reason behind this effect is the assumption of $RK4$ stepping method that functions, which $RK4$ is approximating, are smooth. With higher number of segments, there is higher chance for the ring to be non-smooth, which leads to an exponential errors in $RK4$ algorithm.

Therefore, we propose also a lower boundary δ_{\min} , ensuring the stability, in a following test in next subsection.

Stability test

Stability of simulation in time was measured for a range of resolutions $\delta \in \langle 10, 100 \rangle \mu\text{m}$ and three values of vortex radius $R \in \{500, 1000, 2000\} \mu\text{m}$ using *Euler* and *RK4* stepping method. In all cases, the stability is measured by the maximal number of elapsed epochs, till the simulation was forced to stop. This enforcement was determined by the violation of length condition, as was described in **Real-time tests** subsection- the real vortex circumference $l = \sum_j |\mathbf{s}_j - \mathbf{s}_{j+1}|$ cannot deviate more than 1% from the geometrical value $2\pi R$, where R is the measured radius in current state.

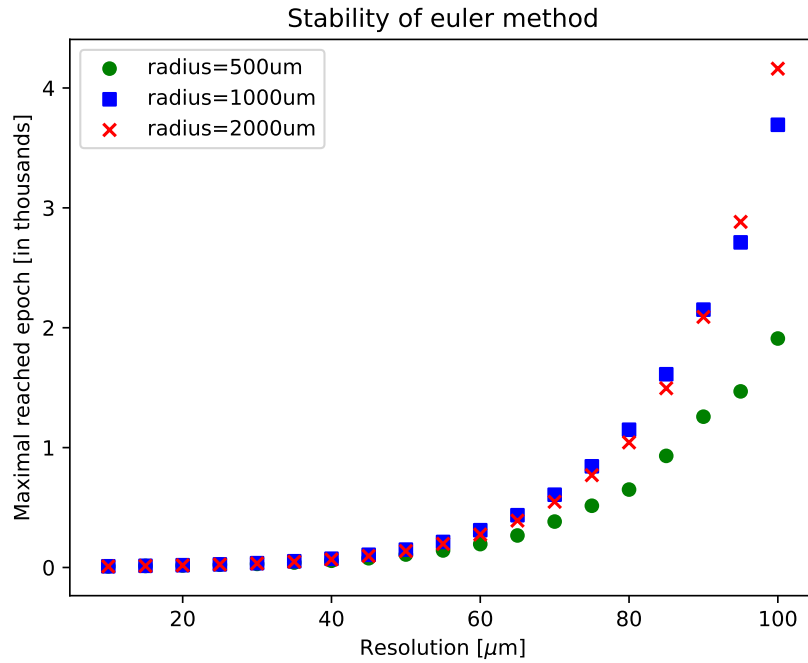


Figure 4.4: Plot of maximal elapsed epoch (time step) of simulation with a given resolution δ , radius R and *Euler* stepping method, till the simulation was forced to stop by violating the length condition.

From the plot in **Figure 4.4**, the *Euler* method seems to be unstable for whatever resolution $\delta \in \langle 10, 100 \rangle \mu\text{m}$. Such behaviour was expected and simulated only as an

example of really wrongly chosen stepping method.

The next experiment was conducted with $RK4$ method, a much stable method comparing with the *Euler* one, but also suffering from strong assumptions (smoothness of evolving function). Nevertheless, the plot of maximal reached epoch performed is much more stable:

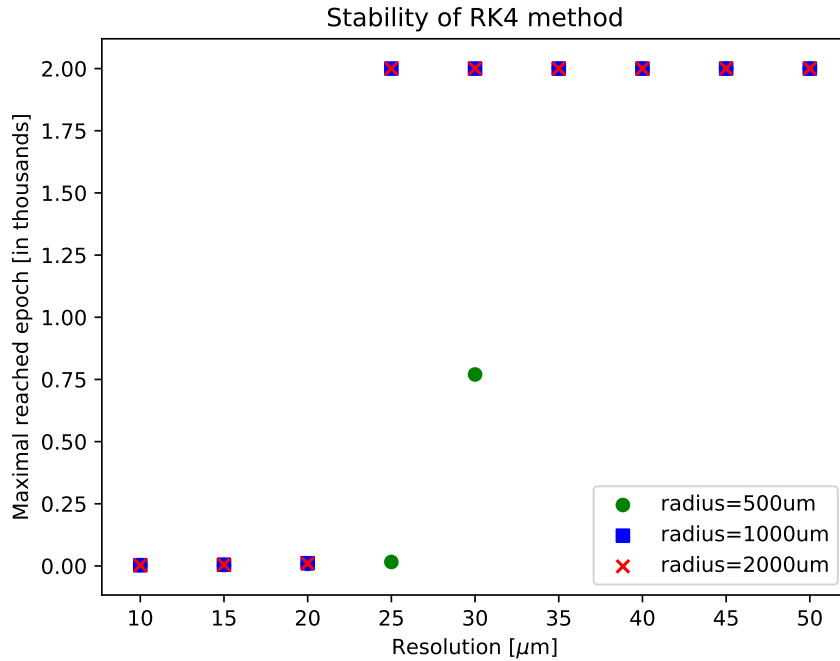


Figure 4.5: Plot of maximal elapsed epoch (time step) of simulation with a given resolution δ , radius R and $RK4$ stepping method, till the simulation was forced to stop by violating the length condition. A threshold is set on 2000 epochs.

The plot in **Figure 14** suggests the minimal resolution to be at least $\delta > 30\mu\text{m}$. This boundary estimate is still quite conservative, since the radius of vortex is decreasing in time and resegmentation processes will happen. Resegmentation process heavily help to the stability of simulation since the deletion of some segments works as a *smoothing effect* which supports the $RK4$ method to be stable.

4.2 Drag force experiments

It was shown in previous works [3] [19] with tuning forks submergeng in Helium-II that it is important to perform full *frequency sweeps* across the resonant response of an oscillator in order to reveal relevant details about any nonlinear effects.

However, these frequency sweeps, at fixed source drive, are heavily time-consuming and sometimes it is useful (especially when we are confident about present laminar mode) to use an *amplitude sweep* with changing drives, a fixed resonant frequency.

Since many hydrodynamic features could be overlooked by using pure amplitude sweeps, we therefore focus in our analysis mainly on the frequency sweeps.

!!TODO!! Force, vel, Drag coeffs, Reynolds, Donnelly graphs

Universal Scaling

!!TODO!! prove universal scaling

Flow phase diagram

!!TODO!! graph of merged fund and overtone modes

5. Conclusions (2 pgs)

- summarize mainly what have we done
- repeat motivations and goals
- list of achievements
- list of failures
- list of improvements
- last words

Bibliography

- [1] TISZA, L. *The viscosity of liquid helium and the Bose-Einstein statistics.* Comptes Rendus Acad. Sciences, **207**:1186-1189 (1952)
- [2] LANDAU, L.D. *The theory of superfluidity of helium II* J. Phys. USSR, Vol. **11**, 91 (1947)
- [3] BAHYL, J. *Measurement of quantum turbulence in superfluid He-4.* Student conference, FMPH UK, Bratislava (2016)
- [4] JACKSON, M.J., SCHMORANZER, D., ET AL. *Universal Drag Force Scaling in High Stokes Number Oscillatory Flows of He II.* Phys Rev B, **submitted** (2018)
- [5] RAYFIELD, G.W., REIF F. *Quantized Vortex Rings in Superfluid Helium* Phys. Rev. A, **136**, 5A (1964)
- [6] FEYNMAN, R. *Application of quantum mechanics to liquid helium.* Prog. in Low Temp. Phys., **1**, 17-53 (1955)
- [7] PENROSE, O., ONSAGER, L. *Bose-Einstein condensation and liquid helium.* Phys. Rev., **104**, 576 (1956)
- [8] VINEN, W.F. and HALL, H.E. *The theory of mutual friction in uniformly rotating helium II.* Proc. Royal Soc. London **238** (1957) 204
- [9] DONNELLY, R.J., BARENGHI, C.F *The Observed Properties of Liquid Helium at the Saturated Vapor Pressure.* American Ins. of Phys. and Chem. Soc. (1998)
- [10] ROBERTS, P.H. Phys. Rev. A, 55 (1971)
- [11] DONNELLY, R.J. *Quantized Vortices in Helium II.* Cambridge studies in low temp. phys. (2005)
- [12] OSBORNE, D.V. *The Rotation of Liquid Helium-II.* Proc. Royal Soc. London , **63**: 909-912 (1950)
- [13] VAN DYKE, M. *An Album of Fluid Motion.* The Parabolic Press, Stanford, California (1982). ISBN 0-915760-02-9
- [14] SCHMORANZER, D., KRÁLOVÁ, V., ET AL. Phys. Rev. E, 81 (2010)
- [15] NICHOL, H.A., SKRBEK, L. ET AL. Phys. Rev. Lett. **92** (2004).

- [16] HOLT, S., SKYBA, P. Rev. Sci. Instrum., **83** (2012)
- [17] GUÉNAULT, A.M., KENNEDY, S.G., ET AL. J, of Low Temp Phys., **62** (1986)
- [18] BLAAUWGEERS, R. BLAŽKOVÁ, M. and col. *Quartz tuning fork: Thermometer, Pressure- and Viscometer for Helium Liquids* J. of Low Temp Phys., Vol. **146** (2007)
- [19] BRADLEY, D.I., ČLOVEČKO, M. and col. Phys. Rev. B **85** (2012)
- [20] SCHMORANZER, D., JACKSON. M.J., ET AL. *Multiple critical velocities in oscillatory flow of superfluid ^4He due to quartz tuning forks.* Phys. Rev. B **94** (2010)
- [21] BAHYL, J. *Measurement of Quantum Turbulence in Superfluid Helium Using Second Sound Attenuation.* Bachelor Thesis, FMPH UK, Bratislava (2016)
- [22] SCHWARZ, K.W. *Three-dimensional vortex dynamics in superfluid He 4: Homogeneous superfluid turbulence*
Phys Rev B, Vol. **38**, 4 (1988)
- [23] TSUBOTA, M., FUJIMOTO, K., YUI S. *Numerical Studies of Quantum Turbulence.* Journal of Low Temp Phys, 188 (2017)
- [24] BAGGLEY, A.W., BARENGHI, C.F. *Spectrum of turbulent Kelvin-waves cascade in superfluid helium.*
Phys Rev B, Vol. **83**, 4 (2011)
- [25] SAMUELS, D.C. *Superfluid vortices and Turbulence.* Quantized Vortex Dynamics and Superfluid Turbulence, Chap.9 (2001)
- [26] BARENGHI, F. *Superfluid vortices and Turbulence.* Quantized Vortex Dynamics and Superfluid Turbulence, Chap.1 (2001)
- [27] BAGGLEY, A.W., BARENGHI, C.F. *Tree Method for Quantum Vortex Dynamics.* Journal of Low Temp Phys, 166 (2012)
- [28] BARNES, J., HUT, P. *A hierarchical $O(N \log N)$ force-calculation algorithm.* Nature, **324**, 446 (1986)